Supplementary Information (SI) for ChemComm.
This journal is © The Royal Society of Chemistry 2026

Supplementary Information

Central-metal-cation-based modulation of gas adsorption selectivity in porous tetrapyrrolic materials

Subrata Maji,[a] Prachi Gupta,[b] Rob Clowes,[b] Yoshitaka Matsushita,[c] Lok K. Shrestha,[a] Anna G. Slater,[b] Jonathan P. Hill,[a] Mandeep K. Chahal*[d]

General Experimental

Reagents and dehydrated solvents (in septum-sealed bottles) used for syntheses and spectroscopic measurements were obtained from Fluorochem, Fischer Scientific, Tokyo Chemical Industry, Wako Chemical Co. or Aldrich Chemical Co. and were used without further purification. Electronic absorption spectra were measured using JASCO V-570 UV/Vis/NIR spectrophotometer or Princeton Applied Research (PAR) diode array rapid scanning spectrometer. ATR-FTIR spectra were obtained using a Thermo-Nicolet 760X FTIR spectrophotometer equipped with a SMART-iTX ATR accessory. ^{1}H-NMR spectra were obtained using a JEOL AL400SSS spectrometer operating at 400 MHz using tetramethylsilane as an internal standard. Proton decoupled ^{13}C-NMR spectra were obtained using a JEOL AL400SSS spectrometer operating at 101 MHz using tetramethylsilane as an internal standard. Data was processed on Delta version 5.0.5.1, Always JNM-AL version 6.2 and MestReNova 6.0.2. ^{1}H NMR chemical shifts (δ) are reported in ppm relative to TMS for $CDCl_3$ (δ 0.00) or the residual solvent peak for other solvents. ^{13}C NMR chemical shifts (δ) are reported in ppm relative to the solvent reported. Coupling constants (*J*) are expressed in Hertz (Hz), shift multiplicities are reported as singlet (s), doublet (d), triplet (t), quartet (q), double doublet (dd), multiplet (m) and broad singlet (bs). High resolution electrospray ionization time-of-flight mass spectra (ESI-TOF-MS) were measured using a Thermo Scientific Q-Exactive Plus instrument and Bruker micrOTOF-Q instrument. Thermogravimetric analyses (TGA) measurements were performed using a Netsch STA2500 Regulus instrument with samples contained in alumina pans using a similar weight of alumina as reference. PXRD measurements were collected in transmission mode from loose powder samples held on thin Mylar film in stainless steel well plates on a PANalytical Empyrean MPD equipped with a high throughput screening (HTS) XYZ stage, X-ray focusing mirror, and PIXcel detector, using Cu Kα (λ = 1.541 Å).

Tetrakis-(3,5-di-*t*-butyl-4-hydroxyphenyl) porphyrin[T(DtBHP)P], Tetrakis-(3,5-di-*t*-butyl-4-hydroxyphenyl) porphinatocopper(II) ([T(DtBHP)P]Cu), 2-formyl-meso-tetrakis-(3,5-di-*t*-butyl-4-hydroxyphenyl) porphyrinatocopper(II) ([T(DtBHP)P]Cu-CHO), H2-OX1 (**2**), Ni-OX1 (**3**), Zn-OX1 (**5**), and Ni-Ox3 (**6**) were prepared according to literature methods.[S1-S3]

X-Ray Crystallography

Crystals were grown by slow evaporation of individual solutions of Cu-OX1 (**1**) and Co-OX1 (**4**) in chloroform. Data collection was performed using MoKα radiation (λ = 0.71073 Å) on a RIGAKU VariMax Saturn diffractometer equipped with a charge-coupled device (CCD) detector. Prior to the diffraction experiment the crystals were flash-cooled to the given temperatures in a stream of cold nitrogen gas. Cell refinements and data reductions were carried out using the d*trek program package in the CrystalClear

software suite.[S4] The structures were solved using a dual-space algorithm method (SHELXT)[S5] and refined by full-matrix least squares on F2 using SHELXL-2014[S6] in the WinGX program package.[S7] Non-hydrogen atoms were anisotropically refined and hydrogen atoms were placed on calculated positions with temperature factors fixed at 1.2 times Ueq of the parent atoms and 1.5 times Ueq for methyl groups. Crystallographic data (excluding structure factors) have been deposited with the Cambridge Crystallographic Data Centre with CCDC reference numbers: 2501550 (Co-OX1 (**4**)) and 2501551 (Cu-OX1 (**1**)). Copies of the data can be obtained, free of charge, on application to CCDC, 12 Union Road, Cambridge CB2 1EZ, UK http://www.ccdc.cam.ac.uk/perl/catreq/catreq.cgi, e-mail: data_request@ ccdc.cam.ac.uk, or fax: +44 1223 336033.

Cu-OX1 (**1**). CCDC reference number 2501550. Crystal data: dull green plate, $C_{83}H_{90}CuN_{10}O_4.1.85(CHCl_3)$, M_r = 1576.02, monoclinic *P1 2$_1$/c 1*, a = 19.665(3) Å, b = 13.997(2) Å c = 32.546(5) Å, V = 8805(2) Å^3, T = 113 K, Z = 4, R_{int} = 0.0649, GoF = 1.758, R_1 = 0.1234, wR(all data) = 0.3806.

Co-OX1 (**4**). CCDC reference number: 2501551. Crystal data: dull dark green plate, $C_{84}H_{91}Cl_3CoN_{10}O_4$, M_r = 1469.94, monoclinic *P1 2$_1$/c 1*, a = 19.623(2) Å, b = 14.1656(15) Å c = 32.426(4) Å, V = 8833.8(16) Å^3, T = 113 K, Z = 4, R_{int} = 0.0561, GoF = 1.052, R_1 = 0.0701, wR(all data) = 0.0771.

Gas adsorption studies

Nitrogen adsorption/desorption isotherms were recorded on a BELSORB Max instrument for the estimation of Brunauer–Emmett–Teller (BET) surface area. Samples were loaded into a cell for measurement and heated at 120 °C under reduced pressure for 24 h prior to collection of the adsorption/desorption isotherms. Nitrogen and Carbon dioxide adsorption/desorption isotherms at 298K and 273 K temperature were carried out on Micromeritics ASAP 2020 surface area and porosity analysers equipped with Julabo circulators and recirculating dewars. Carbon dioxide adsorption/desorption isotherms at 195 K temperature were carried out on a Micromeritics 3Flex gas sorption system equipped with a ColdEdge Technologies Cryostat and SHI Cryogenics Helium compressor. The samples were degassed for 9 h at 110 °C prior to measurement. Between two consecutive measurements, the samples were degassed for 2 h at room temperature.

Synthesis:

Scheme 1

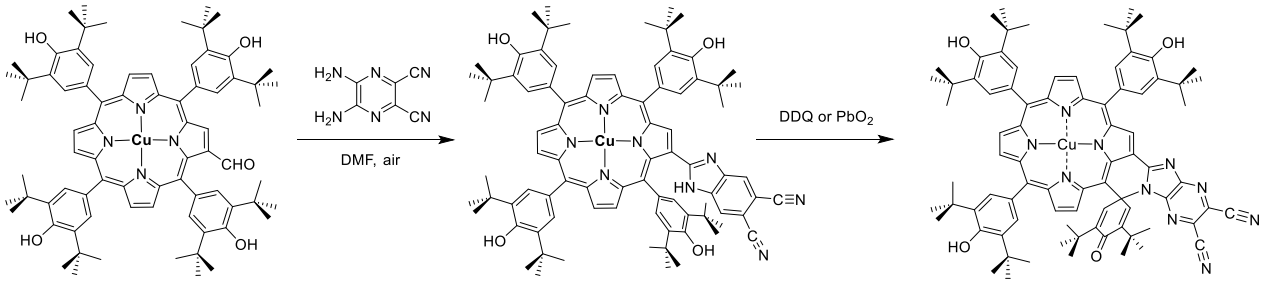

Scheme 2

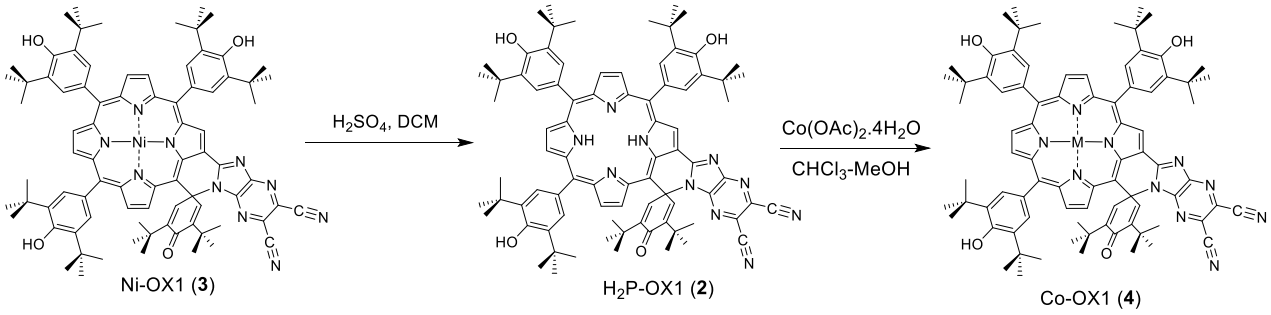

Synthesis Cu-Benzimd, 2-(5,6-Dicyano-1H-imidazo[4,5-b]pyrazin-2-yl)-tetrakis(3,5-di-*t*-butyl-4-hydroxyphenyl)porphyrinatocopper(II)

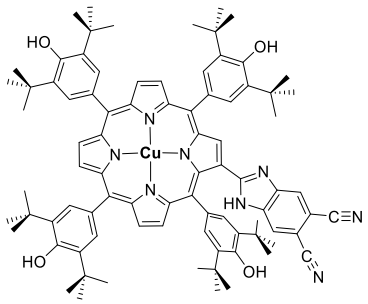

Cu-Benzimd

A mixture of [T(DtBHP)PCu]-CHO[S1] (0.5 g, 0.42 mmol) and 5,6-diamino-2,3-dicyanopyrazine (0.098 g, 0.62 mmol) in dimethylformamide (10 mL) was refluxed under air for 30 h. The reaction mixture was then allowed to cool to room temperature and water was added. The solid precipitate was filtered and dried under reduced pressure. The residue was purified by column chromatography (SiO_2) eluting with hexane/dichloromethane (1:1) to give Cu-Benzimd as a green solid (Yield: 460 mg, 82%).
UV/Vis (CH_2Cl_2): λ / nm (ε / $M^{-1}cm^{-1}$): 232 (59100), 340 (22700), 418 (102400), 560 (12300), 618 (17000).
HRMS (ESI-MS, DCM); calculated for $[C_{83}H_{92}O_4N_{10}Cu]^+$ = 1355.6594, found: = 1355.6365.

Cu-OX1 (**1**)

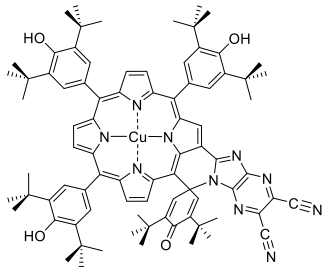

Cu-OX1 (**1**)

Oxidation procedure for the synthesis of Cu-OX1 (**1**) was the same as previously reported for the Ni-complexes using either DDQ or PbO_2 as the oxidant.[S2]

Cu-OX1 (**1**). UV/Vis (CH_2Cl_2): λ / nm (ε / $M^{-1}cm^{-1}$): 232 (77500), 336 (34800), 408 (114400), 476 (161400), 574 (13200), 624 (44800). ^{1}H NMR (400 MHz, $CDCl_3$): δ = Cu(II)-OX1 (**1**) is paramagnetic complex so broad NMR. FT-IR(ATR): ν = 3631.7 (m, OH(str)), 2954.6 (m, CH(str)), 2869.5 (m, CH(str)), 2236.2 (w, C≡N(str)), 1723.4 (w), 1708.4 (w), 1666.0 (w), 1631.7 (s), 1573.7 (w), 1544.4 (w), 1484.0 (w), 1432.2 (s), 1408.9 (s), 1391.9 (w), 1376.5 (w), 1363.5 (w), 1346.3 (m), 1321.2 (m), 1247.5 (w), 1235.8 (m), 1217.5 (m), 1198.3 (w), 1146.6 (w), 1131.7 (m), 1121.0 (m), 1077.7 (w), 1008.1 (s), 956.7 (w), 937.1 (m), 919.8 (w), 888.5 (w), 853.4 (w), 826.0 (w), 803.8 (m), 784.7 (w), 772.5 (w), 756.5 (w), 722.1 (m), 715.4 (m), 678.1 (w), 655.8 (w), 634.5 (w) cm^{-1}. HRMS (ESI-MS, DCM); calculated for $[C_{83}H_{90}O_4N_{10}Cu]^+$ = 1353.6437, found: = 1353.6224.

Co-OX1 (**4**)

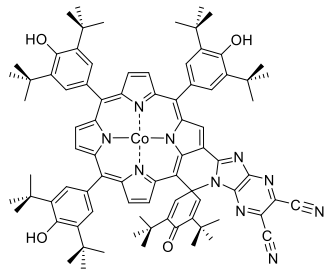

Co-OX1 (**4**)

H2-OX1 (**2**) (80 mg, 0.062 mmol) was dissolved in $CHCl_3$ (15 mL) then $Co(OAc)_2 \cdot 4H_2O$ (154 mg, 0.62 mmol, 10 eq.) dissolved in methanol (3 mL) was added and the resulting mixture refluxed for 1 h. The reaction mixture was cooled to room temperature, washed with water and the organic fraction dried over anhydrous Na_2SO_4. The crude product was purified by column chromatography on silica using $CHCl_3$ as an eluent yielding Co-OX1 (**4**) (75 mg, 90%).

UV/Vis (CH_2Cl_2): λ / nm (ε / $M^{-1}cm^{-1}$): 230 (64100), 402 (108900),470 (112200), 616 (35400).
^1H NMR (400 MHz, $CDCl_3$): δ = Co(II)-OX1 (**4**) is a paramagnetic complex leading to broadened NMR spectra (see Figure S5). FT-IR(ATR): ν = 3634.9 (m, OH(str)), 2954.5 (m, CH(str)), 2911.7 (m, CH(str)), 2870.0 (m, CH(str)), 2233.0 (w, C≡N(str)), 1669.2 (w), 1629.4 (s), 1588.5 (w), 1543.0 (w), 1500.8 (w), 1483.3 (w), 1432.5 (s), 1409.0 (s), 1381.1 (w), 1352.4 (m), 1319.5 (m), 1234.7 (m), 1218.6 (m), 1199.6 (w), 1149.7 (w), 1131.6 (m), 1121.2 (m), 1072.1 (w), 1025.6 (w), 1008.0 (m), 957.1 (w), 938.5 (m), 888.5 (w), 854.1 (w), 819.6 (w), 801.6 (m), 783.1 (w), 772.3 (w), 755.9 (w), 715.1 (m), 691.9 (w), 682.6 (w), 656.1 (w), 633.9 (w) cm^{-1}.
HRMS (ESI-MS, DCM); calculated for $[C_{83}H_{93}O_4N_{10}Co]^+$ = 1352.6708, found: = 1352.6218.

ESI-TOF-MS spectrum of **Cu-Benzimd**

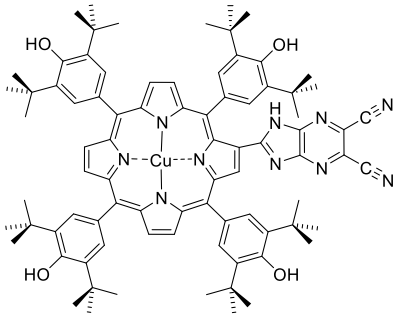

Chemical Formula: $C_{83}H_{92}CuN_{10}O_4$

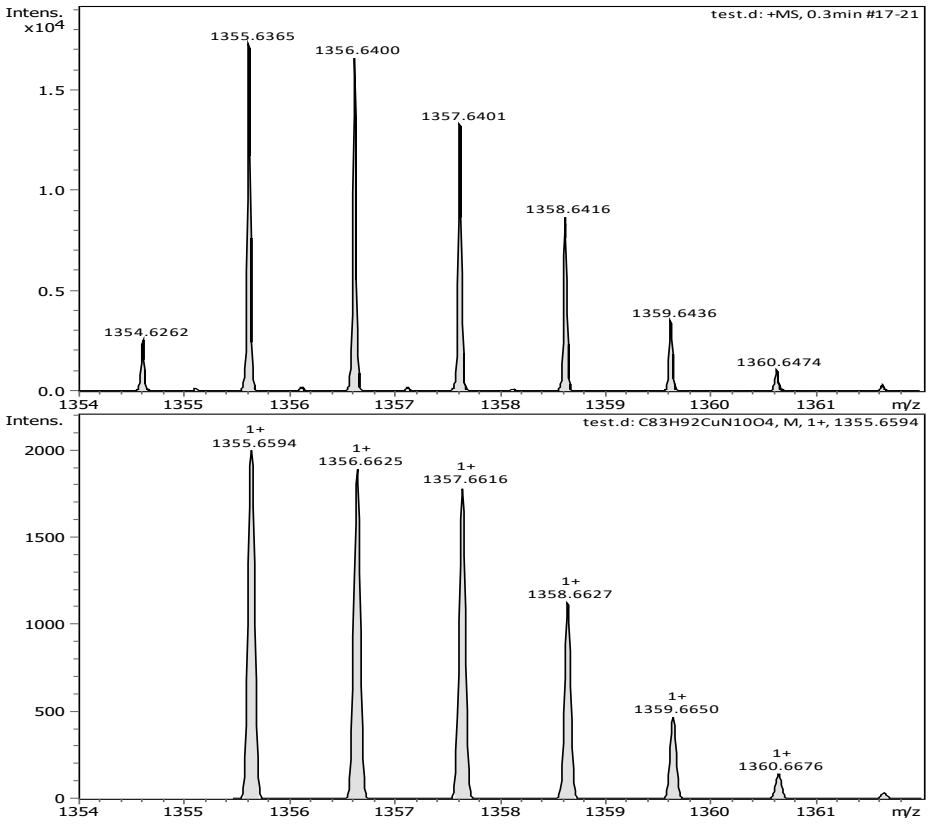

Figure S1. Experimental (upper) and calculated (lower) ESI-TOF-MS for **Cu-Benzimd**.

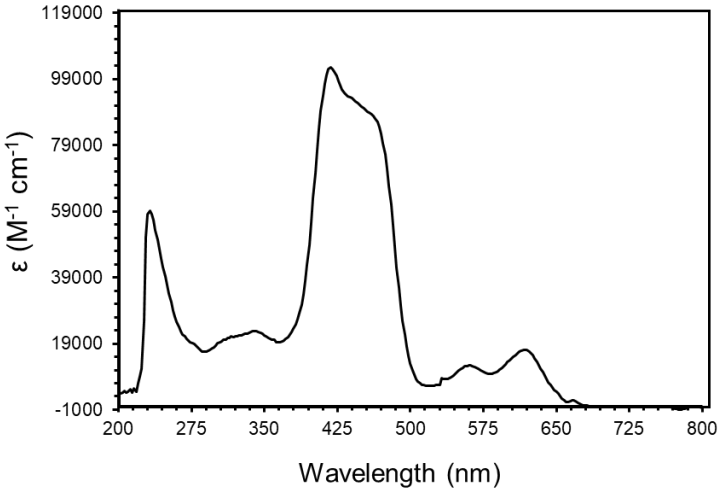

Figure S2. UV-Vis spectrum for **Cu-Benzimd** in CH_2Cl_2.

ESI-TOF-MS spectrum of Cu-OX1 (**1**)

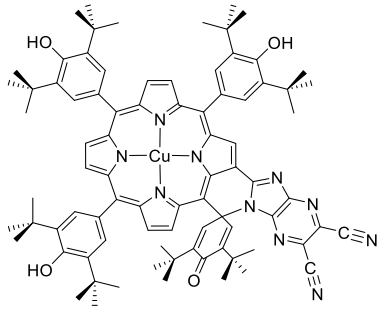

Chemical Formula: $C_{83}H_{90}CuN_{10}O_4$

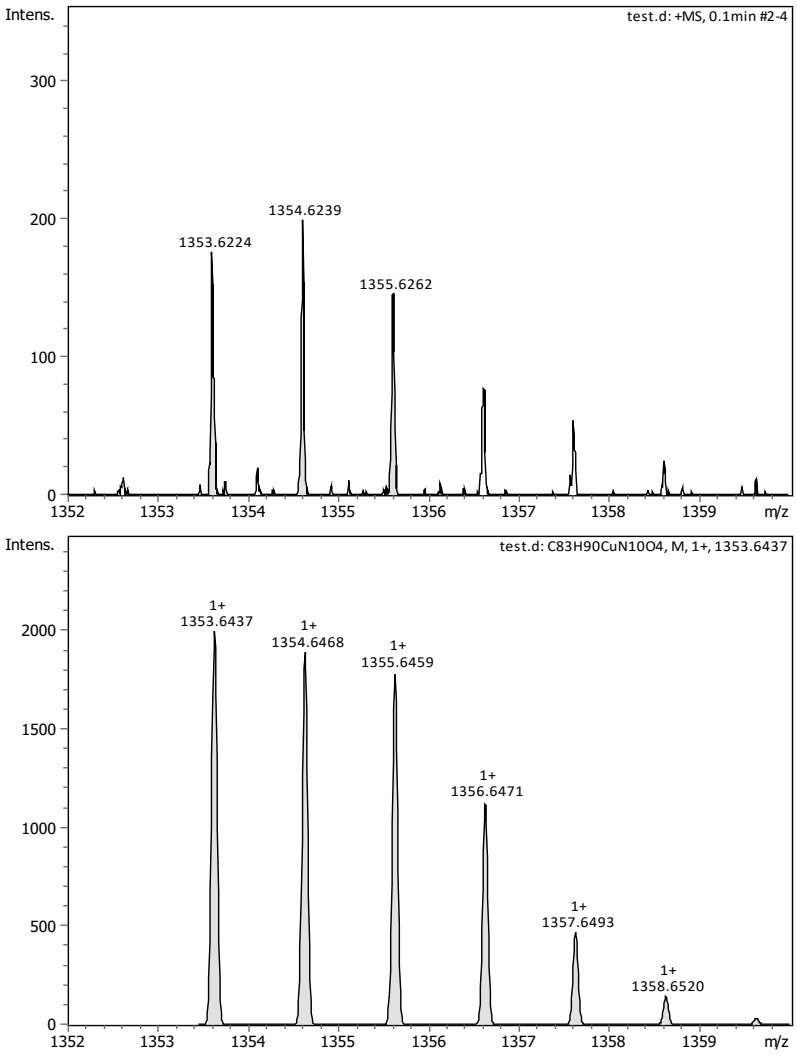

Figure S3. Experimental (upper) and calculated (lower) ESI-TOF-MS of Cu-OX1 (**1**).

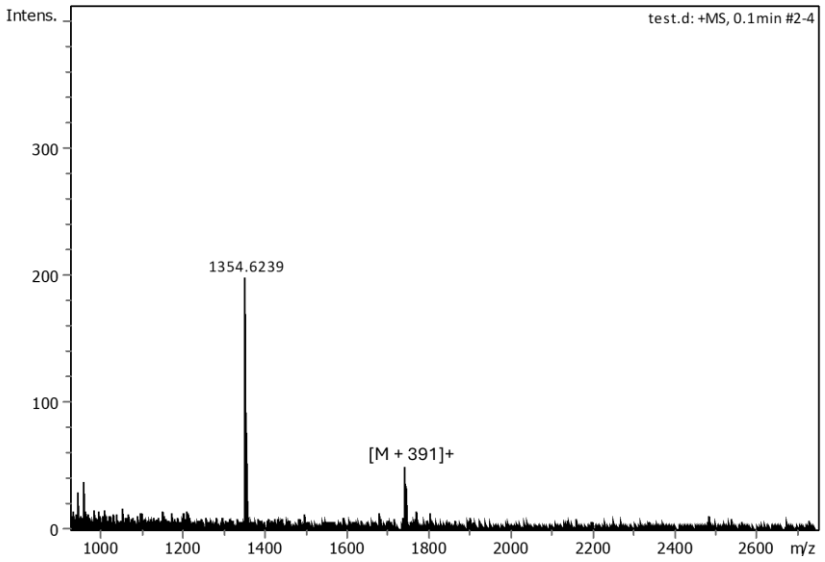

Figure S4. Experimental full range mass spectrum (ESI-TOF-MS) of Cu-OX1 (**1**). Peak [M+391]+ corresponds to [M + plasticizer (common impurity in ESI-MS)].

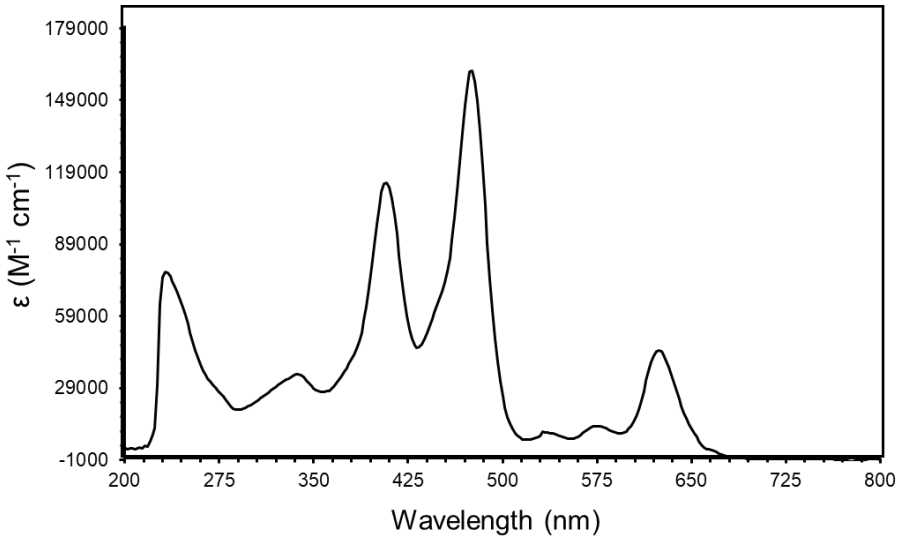

Figure S5. UV-Vis spectrum for Cu-OX1 (**1**) in CH_2Cl_2.

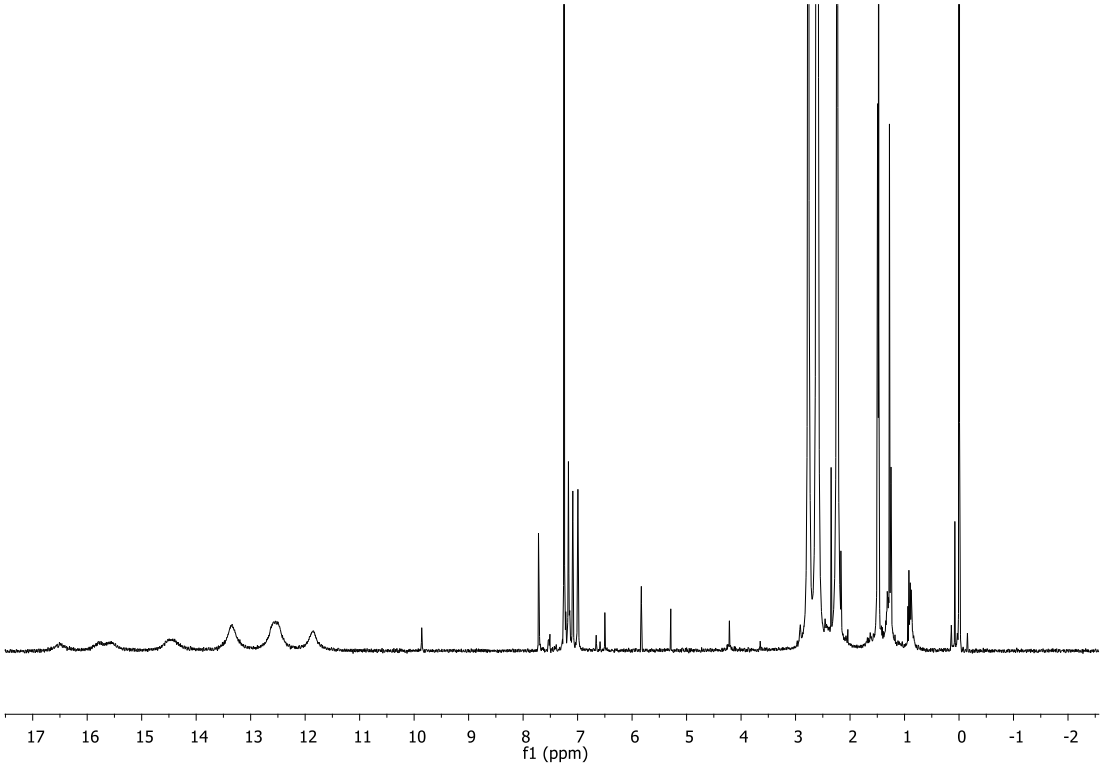

Figure S6. ^{1}H NMR spectrum of Co-OX1 (**4**) in $CDCl_3$.

ESI-TOF-MS spectrum of Co-OX1 (**4**)

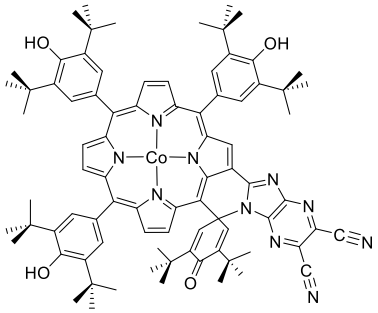

Chemical Formula: $C_{83}H_{90}CoN_{10}O_4$

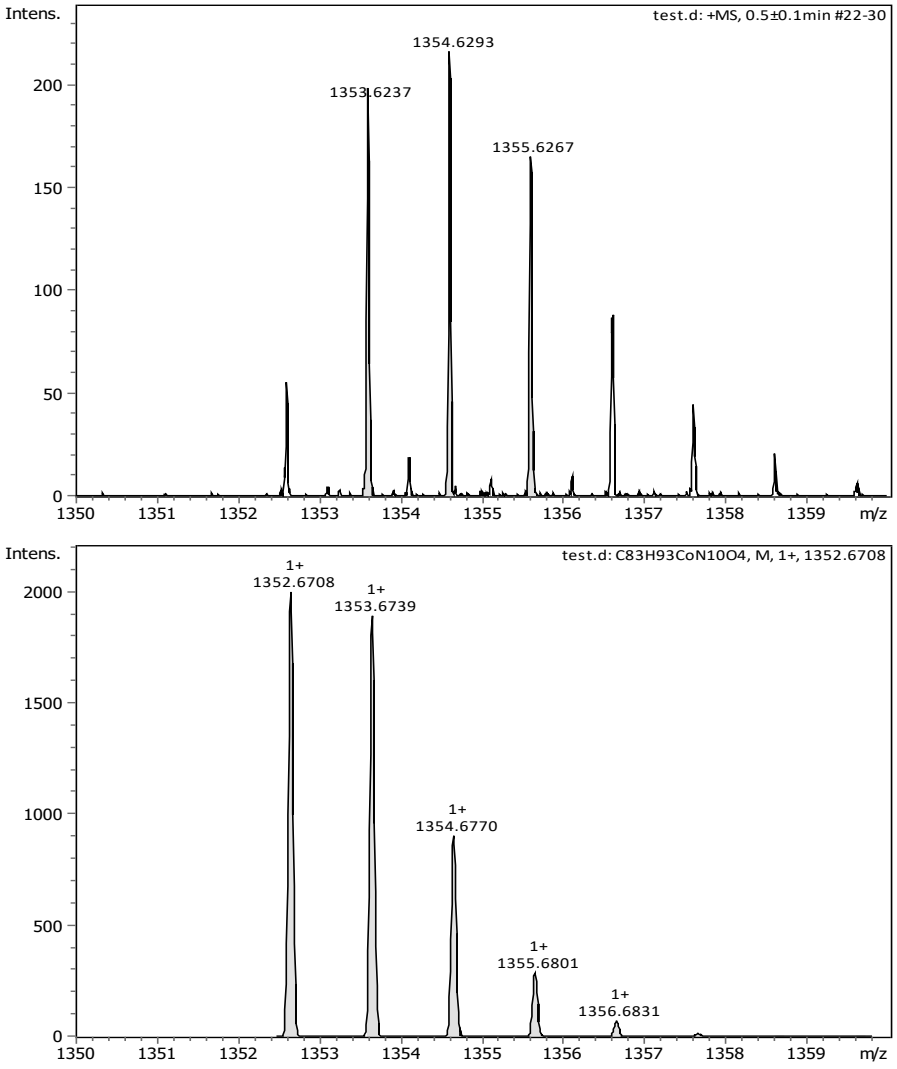

Figure S7. Experimental (upper) and calculated (lower) ESI-TOF-MS of Co-OX1 (**4**).

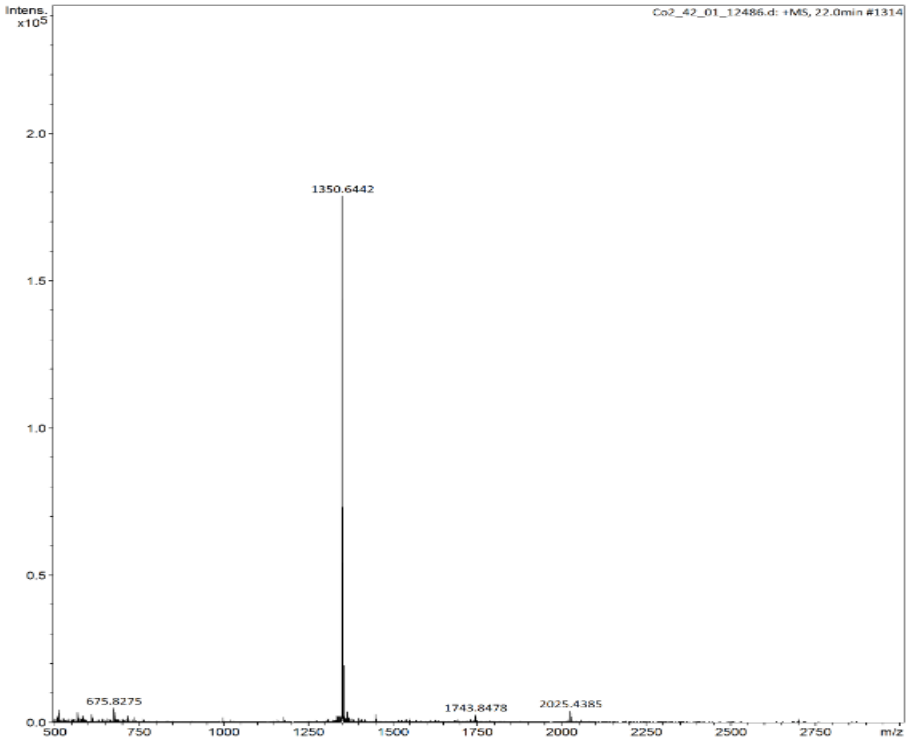

Figure S8. Experimental full range mass spectrum of Co-OX1 (**4**).

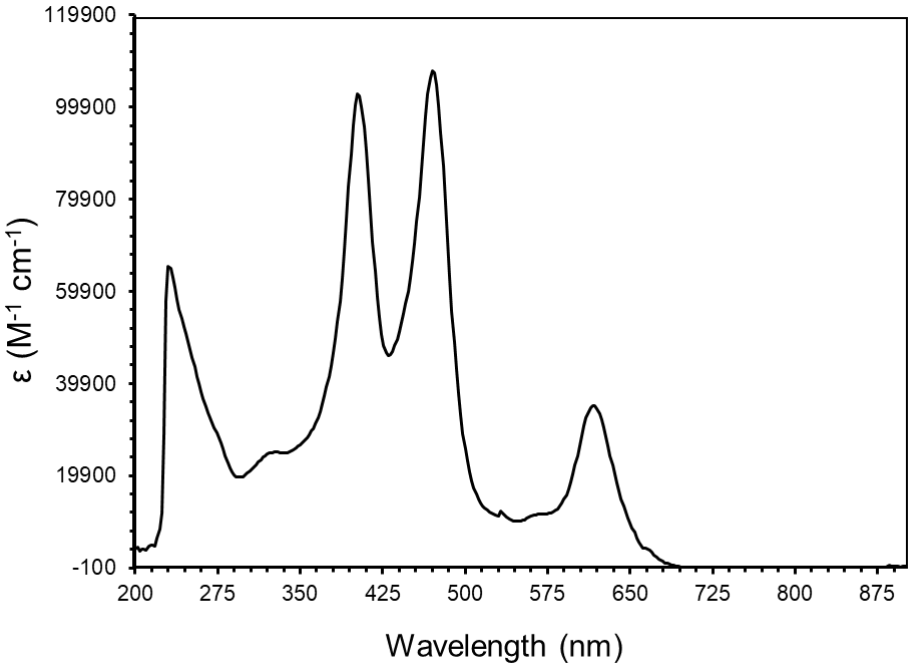

Figure S9. UV-Vis spectrum for Co-OX1 (**4**) in CH_2Cl_2.

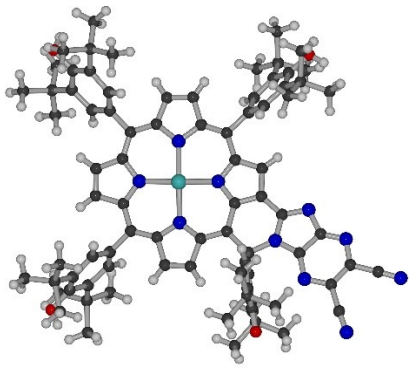

Figure S10. X-ray crystal structure of Cu-OX1 (**1**).

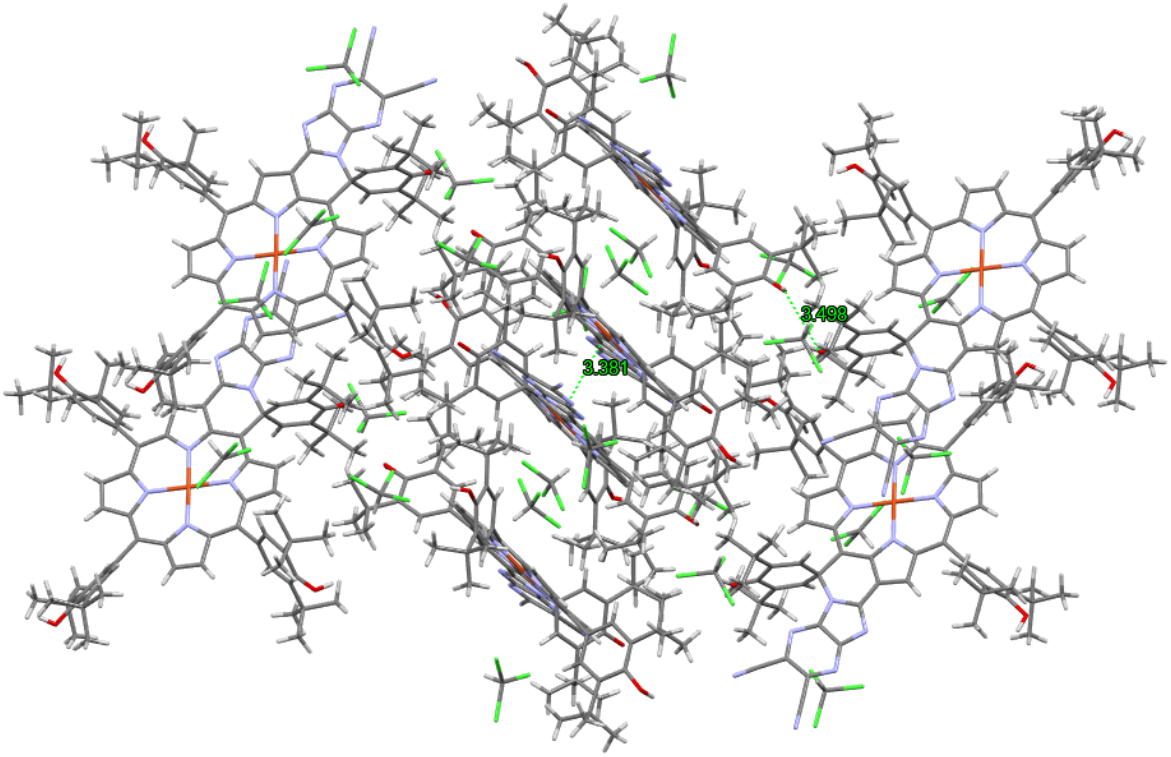

Figure S11. X-ray crystal structure of Cu-OX1 (**1**) showing intermolecular π–π stacking and H-bonding interactions.

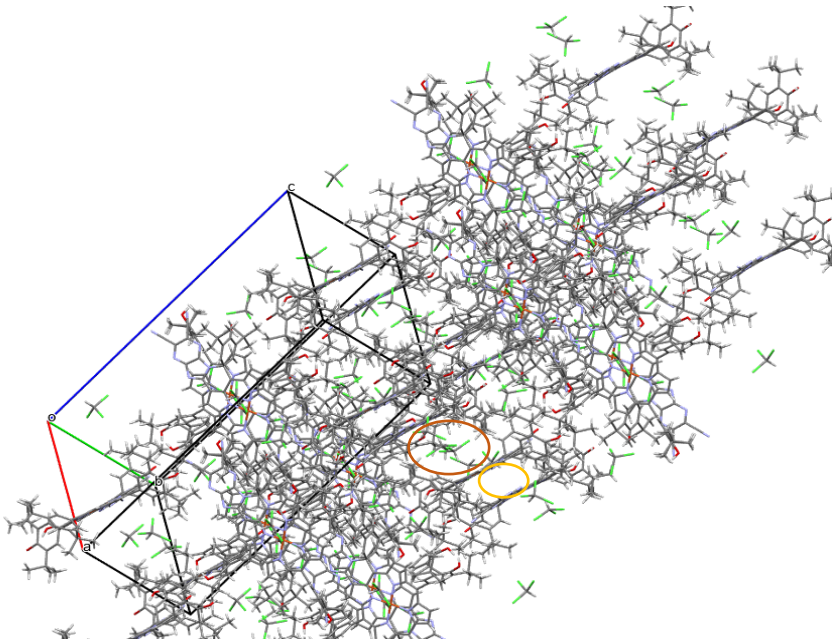

Figure S12. X-ray crystal structure of Cu-OX1 (**1**) showing empty pockets with $CHCl_3$ molecules inside (orange circle) and empty pocket (yellow circle).

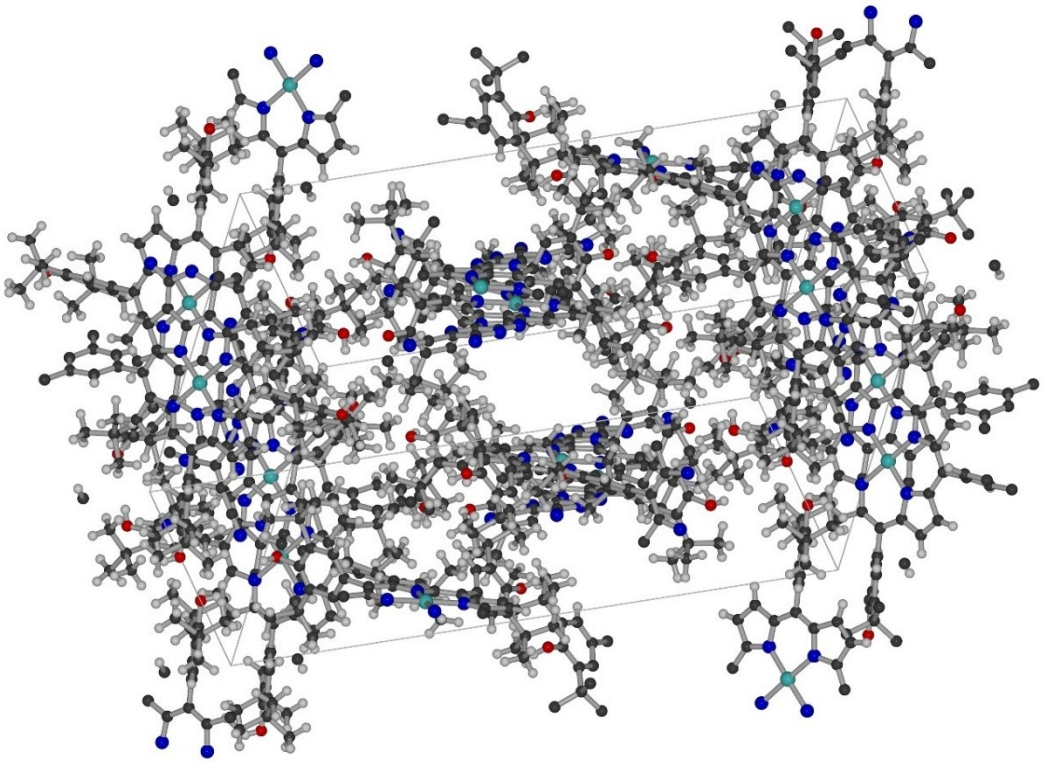

Figure S13. X-ray crystal structure of Cu-OX1 (**1**) showing empty pocket (solvating $CHCl_3$ molecules removed).

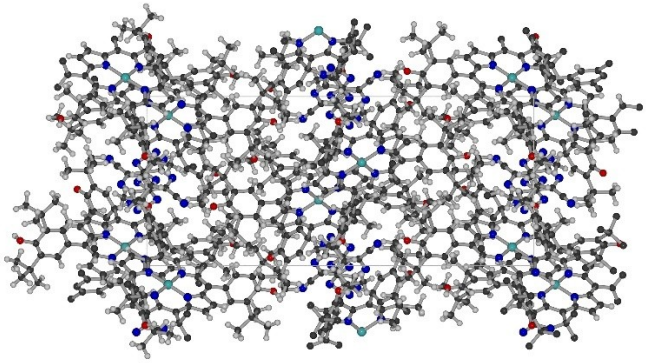

Figure S14. X-ray crystal structure of Cu-OX1 (**1**) viewed along a-axis.

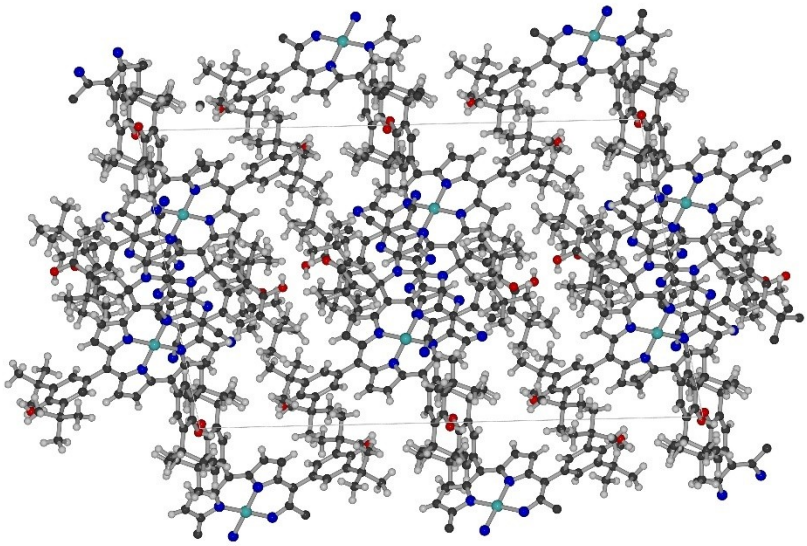

Figure S15. X-ray crystal structure of Cu-OX1 (**1**) viewed along b-axis.

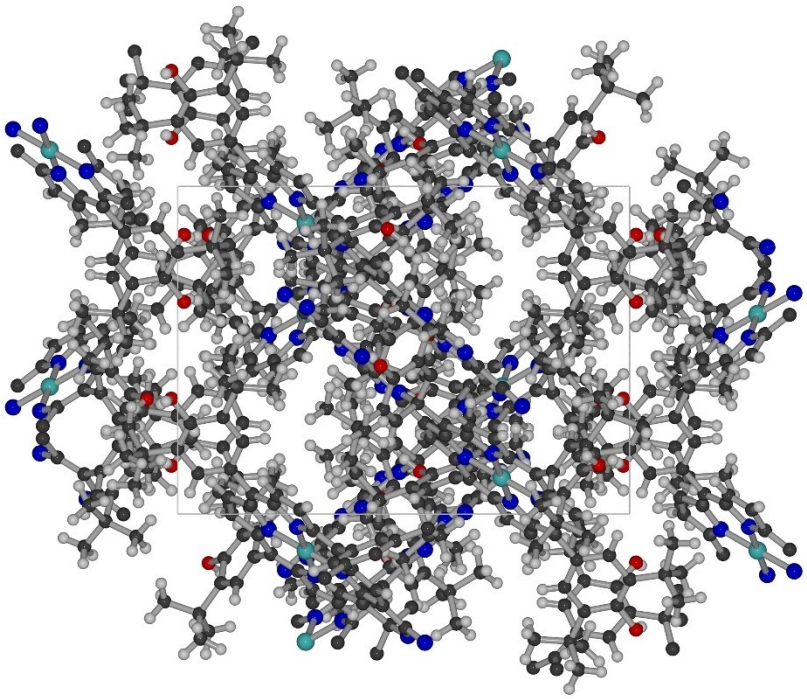

Figure S16. X-ray crystal structure of Cu-OX1 (**1**) viewed along c-axis.

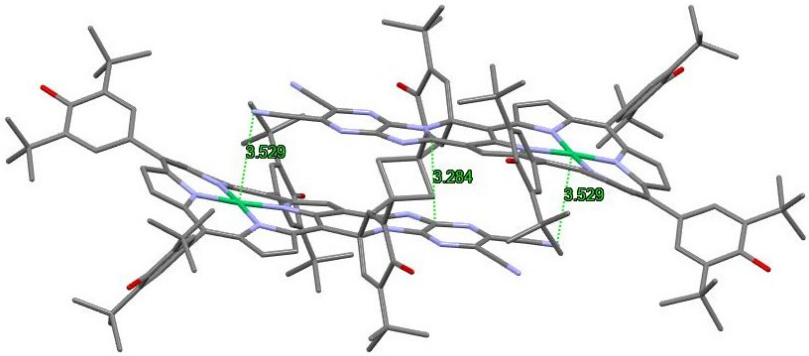

Figure S17. Dimer structure formed by intermolecular π–π stacking of Ni-OX1 (**3**).

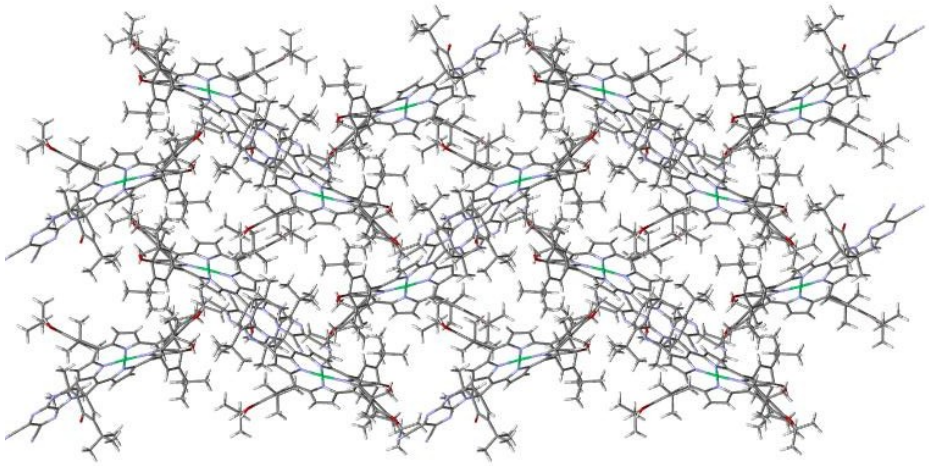

Figure S18. X-ray crystal structure of Ni-OX (**3**) viewed along a-axis.

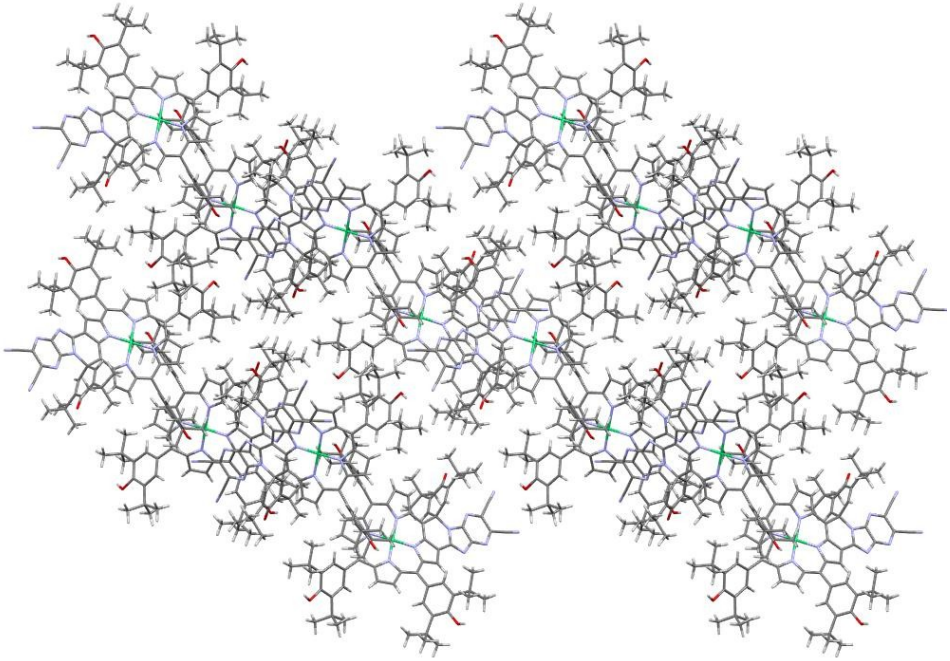

Figure S19. X-ray crystal structure of Ni-OX (**3**) viewed along b-axis.

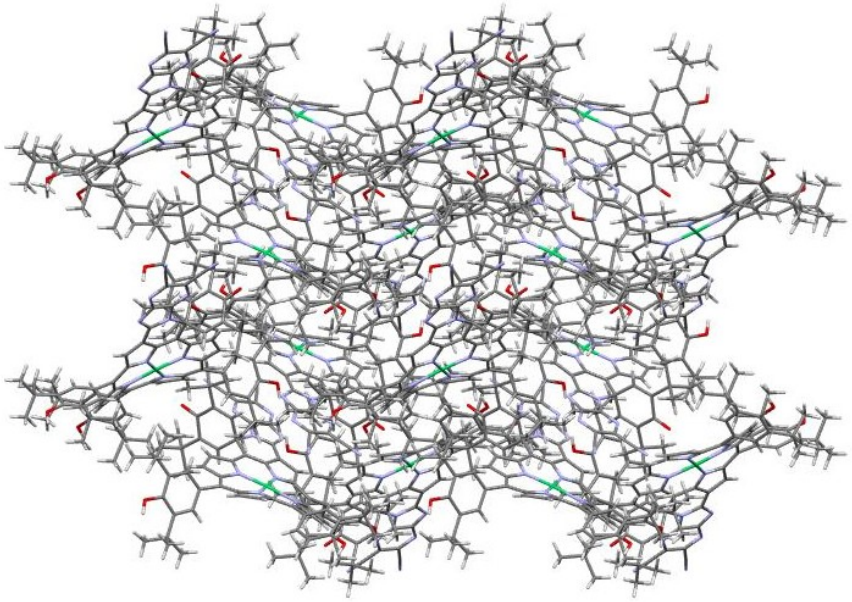

Figure S20. X-ray crystal structure of Ni-OX (**3**) viewed along c-axis.

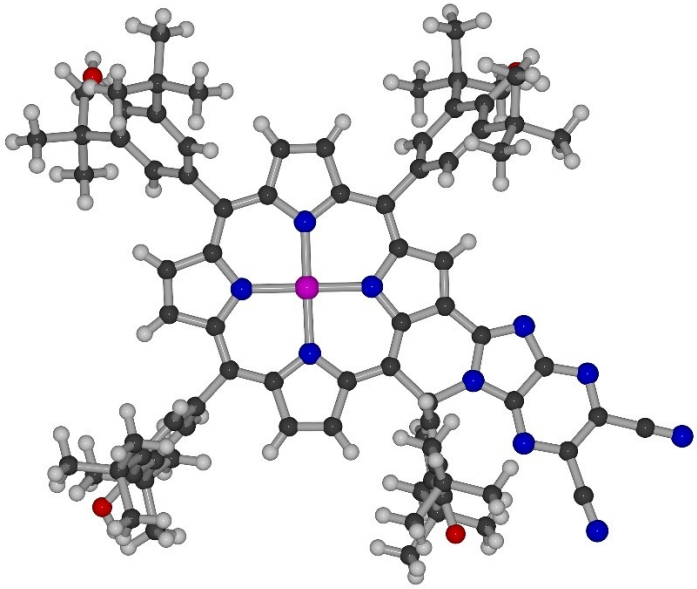

Figure S21. X-ray crystal structure of Co-OX1 (**4**).

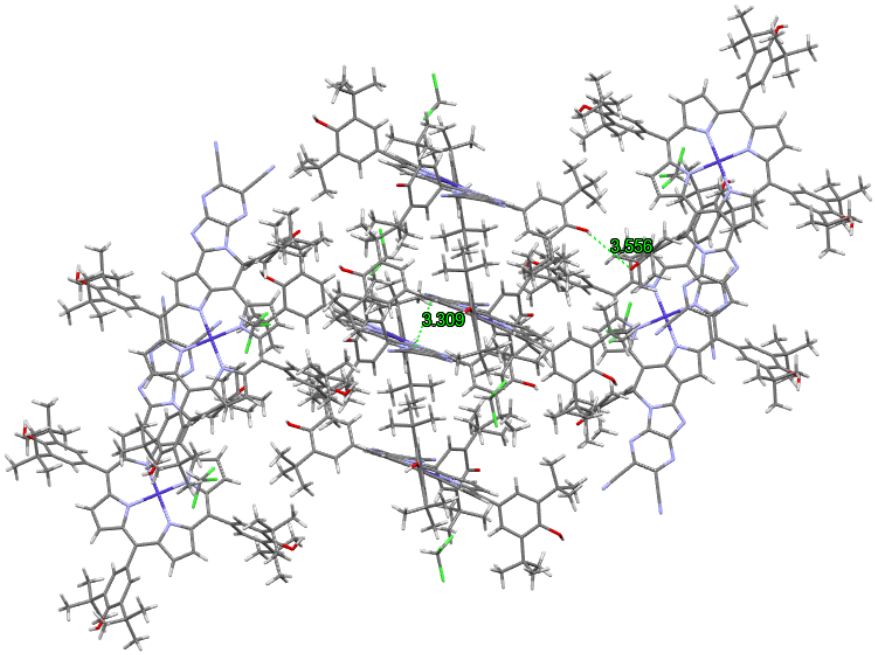

Figure S22. X-ray crystal structure of Co-OX1 (**4**) showing intermolecular π–π stacking and H-bonding interactions.

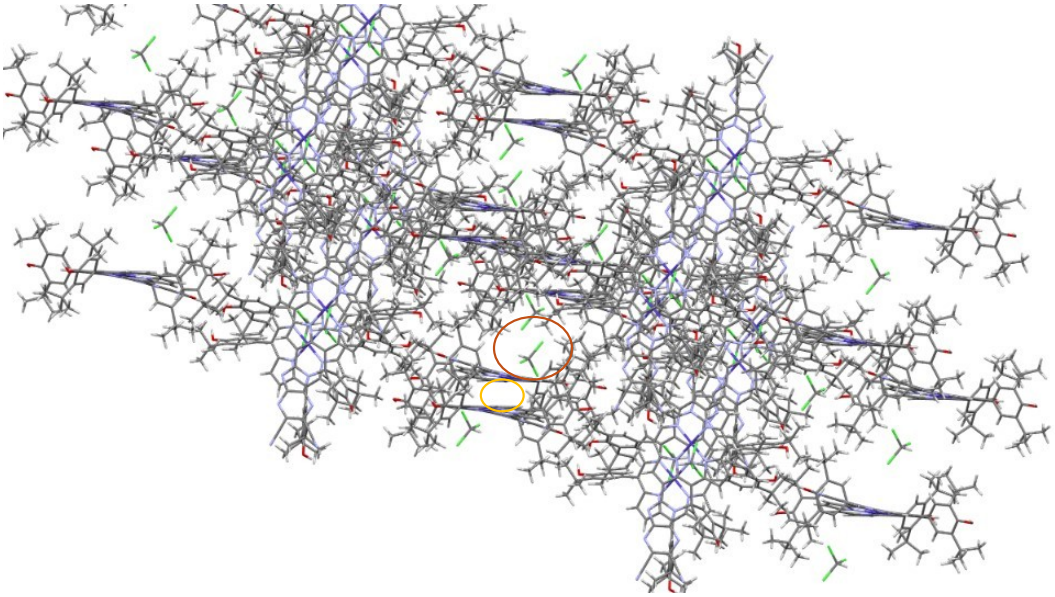

Figure S23. Extended X-ray crystal structure of Co-OX1 (**4**) showing pockets containing solvating $CHCl_3$ molecules (orange circle). Yellow circle denotes the dimer stacking region.

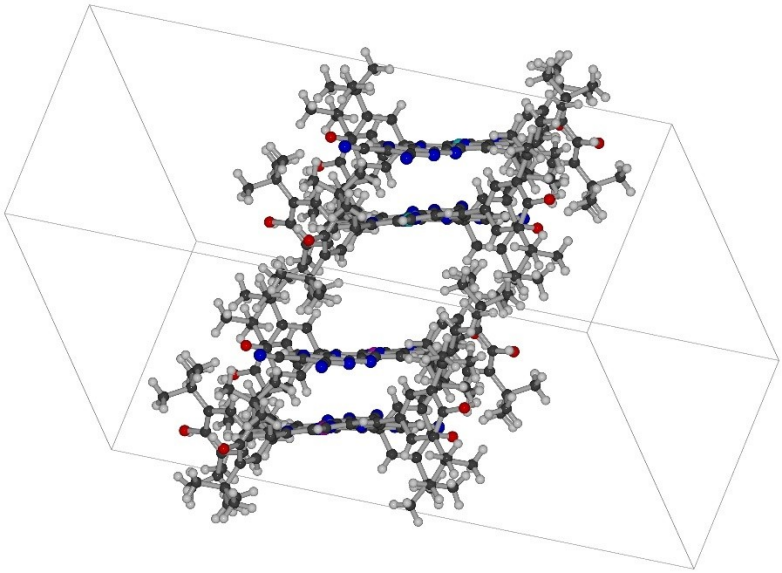

Figure S24. X-ray crystal structure of Co-OX1 (**4**) showing inter-dimer voids (solvent molecules removed).

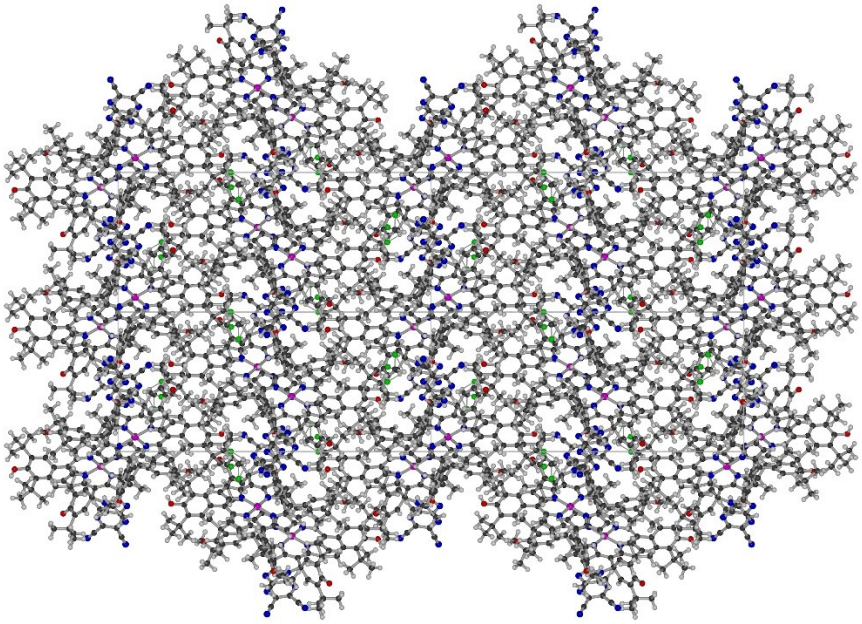

Figure S25. X-ray crystal structure of Co-OX1 (**4**) viewed along a-axis.

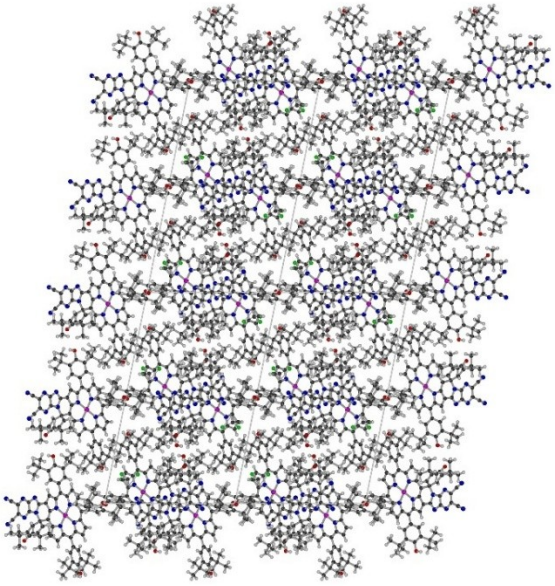

Figure S26. X-ray crystal structure of Co-OX1 (**4**) viewed along b-axis.

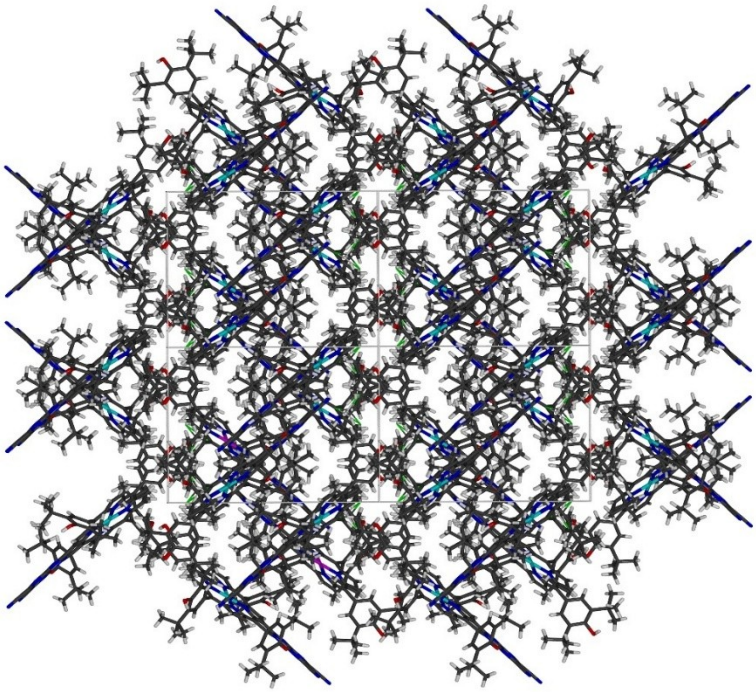

Figure S27. X-ray crystal structure of Co-OX1 (**4**) viewed along c-axis.

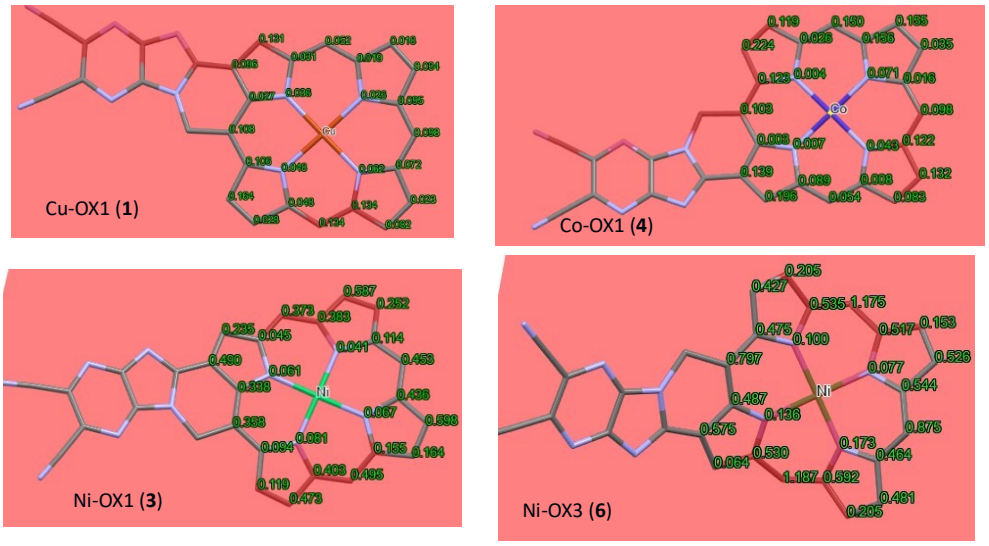

Figure S28. Displacement of porphyrin-core atoms in Å from the mean plane for Cu-OX1 (**1**), Ni-OX1 (**3**), Co-OX1 (**4**) and Ni-OX3 (**6**).

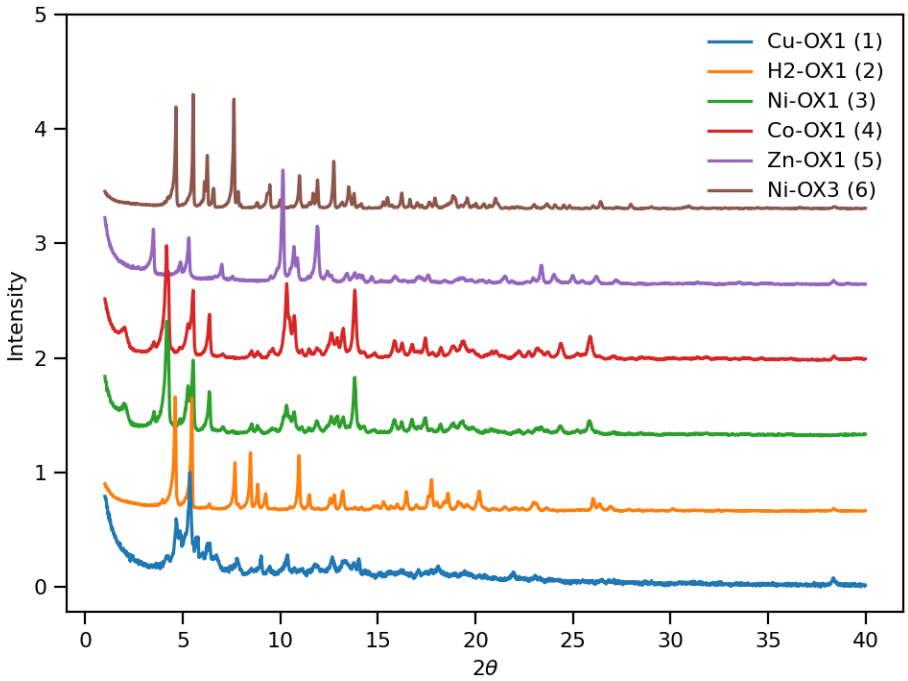

Figure S29. Experimental PXRD patterns (normalized) for Cu-OX1 (**1**), H2-OX1 (**2**), Ni-OX1 (**3**), Co-OX1 (**4**), Zn-OX1 (**5**) and Ni-OX3 (**6**).

Table S1. Porosity properties obtained from DFT and BJH methods.

Sample	SSA ($m^2 g^{-1}$)	S_{micro} ($m^2 g^{-1}$)	S_{meso} ($m^2 g^{-1}$)	V_p ($cm^3 g^{-1}$)	V_{micro} ($cm^3 g^{-1}$)	D_w (nm)	D_p (nm)
Cu-OX1 (**1**)	450.567	414.239	36.328	0.304	0.206	0.287	3.884
H2-OX1 (**2**)	450.710	425.076	25.634	0.296	0.205	0.287	3.875
Ni-OX1 (**3**)	15.119	6.440	8.679	0.040	0.014	1.265	4.106
Co-OX1 (**4**)	509.912	483.068	26.844	0.338	0.264	0.705	3.877
Zn-OX1 (**5**)	346.575	338.305	8.270	0.162	0.128	0.287	3.091
Ni-OX3 (**6**)	343.564	338.651	4.913	0.249	0.210	0.705	3.873

SSA = specific surface area, S_{micro} = micropore surface area, S_{meso} =mesopore surface area, V_p = total pore volume, V_{micro} = micropore volume, D_w = half pore width, and D_p = average mesopore diameter.

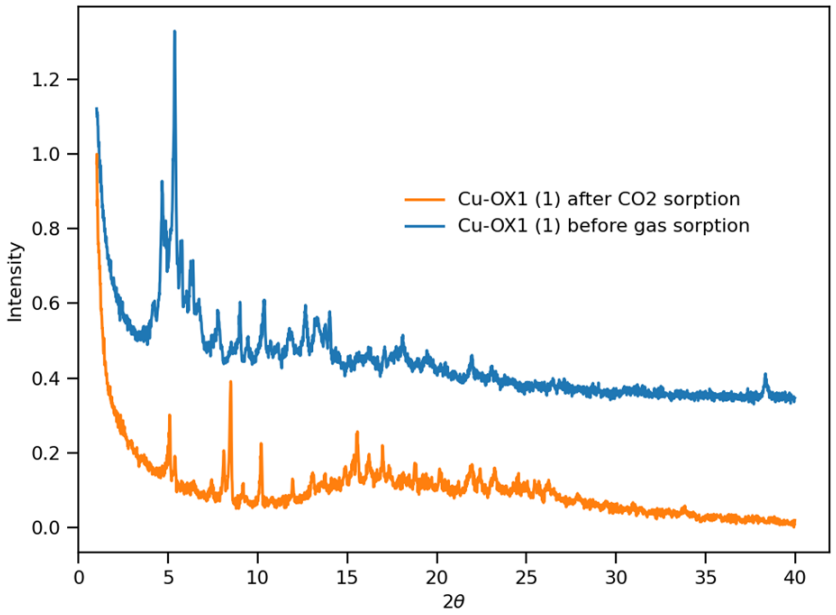

Figure S30. PXRD patterns (normalized) of Cu-OX1 (**1**) as synthesised sample before and after CO_2 uptake studies (sample was degassed for 9 h at 110 °C at the start of gas uptake measurement).

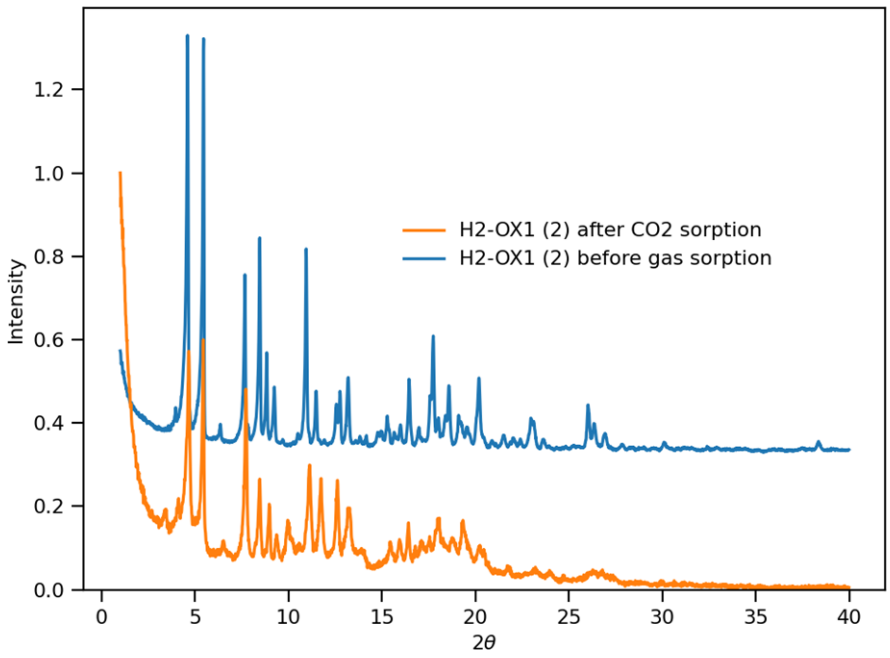

Figure S31. PXRD patterns (normalized) of H2-OX1 (**2**) as synthesised sample before and after CO_2 uptake studies (sample was degassed for 9 h at 110 °C at the start of gas uptake measurement).

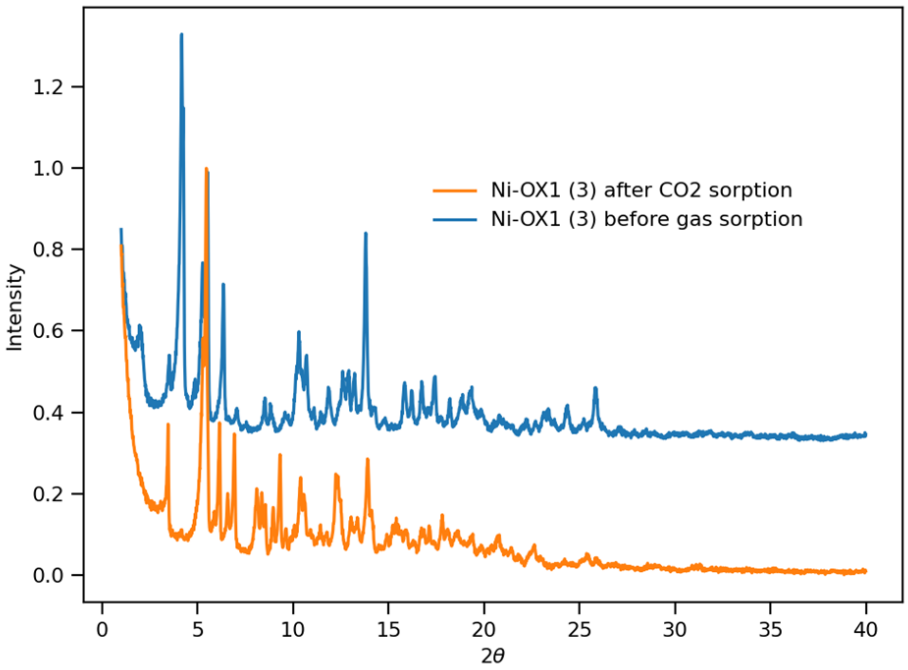

Figure S32. PXRD patterns (normalized) of Ni-OX1 (**3**) as synthesised sample before and after CO_2 uptake studies (sample was degassed for 9 h at 110 °C at the start of gas uptake measurement).

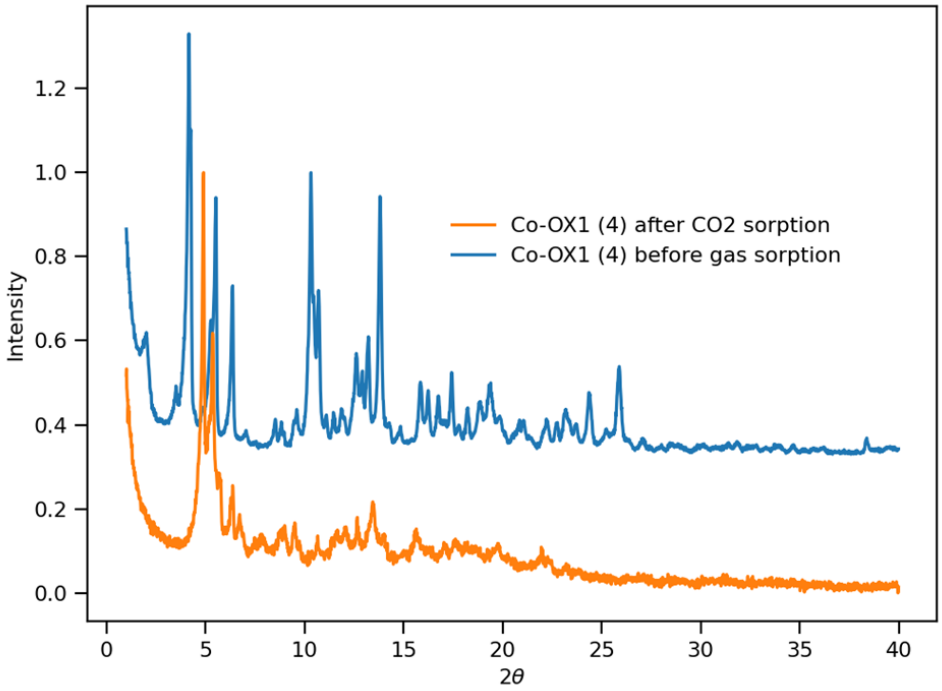

Figure S33. PXRD patterns (normalized) of Co-OX1 (**4**) as synthesised sample before and after CO_2 uptake studies (sample was degassed for 9 h at 110 °C at the start of gas uptake measurement).

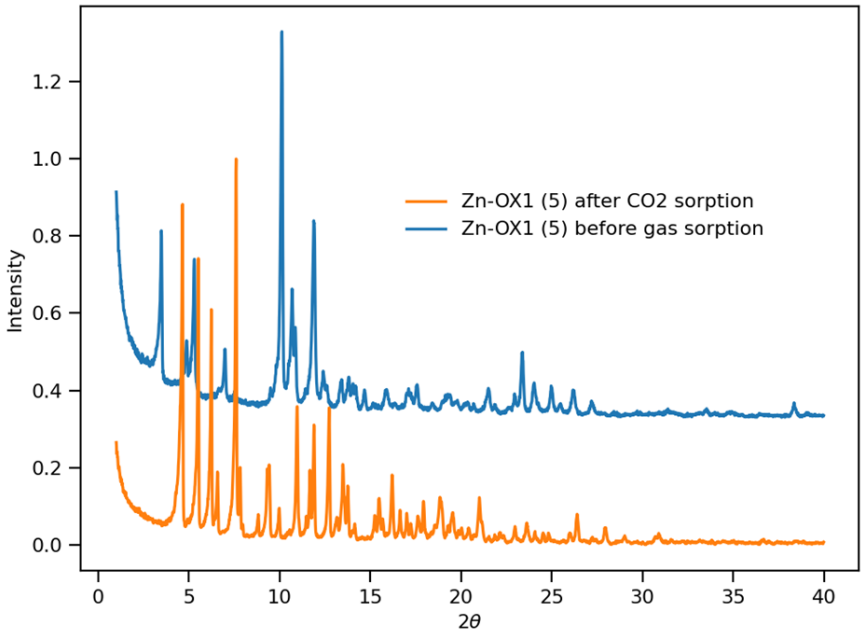

Figure S34. PXRD patterns (normalized) of Zn-OX1 (**5**) as synthesised sample before and after CO_2 uptake studies (sample was degassed for 9 h at 110 °C at the start of gas uptake measurement).

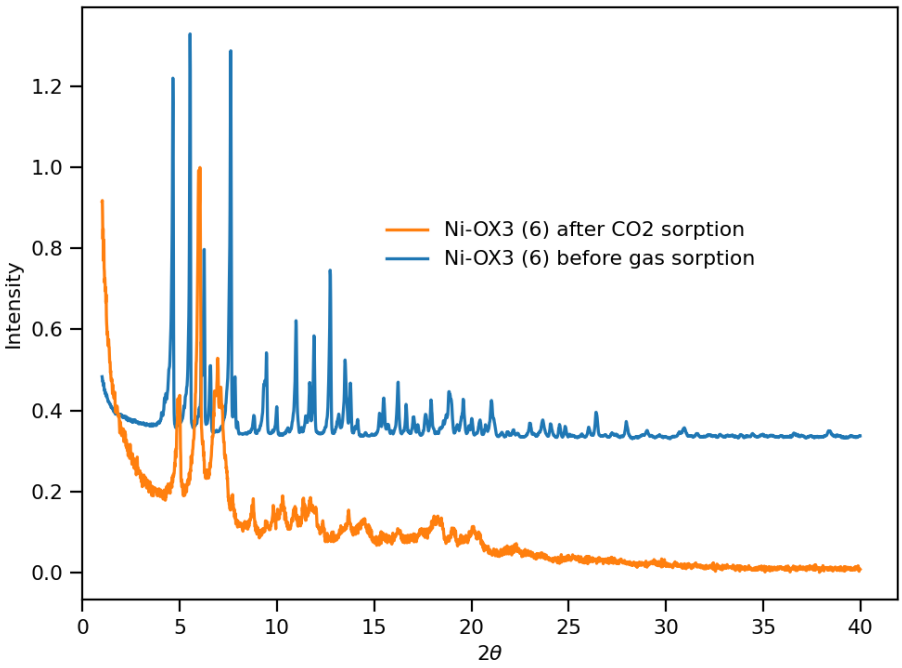

Figure S35. PXRD patterns (normalized) of Ni-OX3 (**6**) as synthesised sample before and after CO_2 uptake studies (sample was degassed for 9 h at 110 °C at the start of gas uptake measurement).

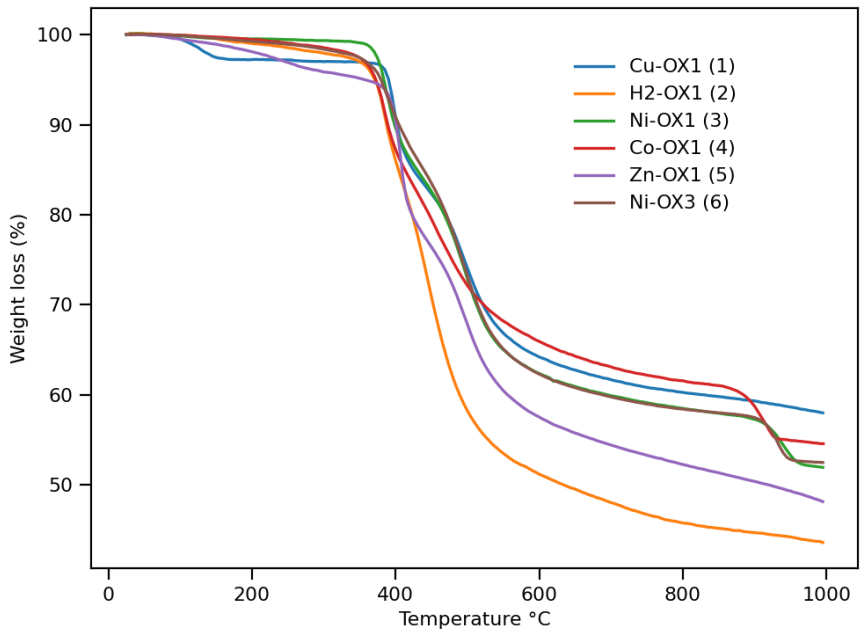

Figure S36. Thermogravimetric analyses (TGA) curves of porphyrin complexes in the range of 25-1000 °C.

Table S2 The CO_2 and N_2 uptake capacities of **M-OX1** and **Ni-OX3** at 273 K and 298K and comparison with literature reported processable porphyrinic porous organic molecular materials.

Porphyrinic porous material	CO_2 uptake at 273K ($cm^3\ g^{-1}$)	CO_2 uptake at 298K ($cm^3\ g^{-1}$)	N_2 uptake at 273K ($cm^3\ g^{-1}$)	N_2 uptake at 298K ($cm^3\ g^{-1}$)
Cu-OX1 (**1**)	47.06	35.76	7.39	4.41
H2-OX1 (**2**)	**67.65**	30.04	5.36	0.38
Ni-OX1 (**3**)	27.61	21.96	3.39	2.37
Co-OX1 (**4**)	46.67	**51.66**	8.95	5.27
Zn-OX1 (**5**)	41.79	30.28	4.99	3.37
Ni-OX3 (**6**)	17.59	11.57	2.21	1.86
UPC-H4a[S8]	<15	<15		
FDU-HOF-2[S9]		25.8		
PFC-5[S10]	32.8	23.9		
HOF-7a[S11]	<15	<15 (296K)		
HOF-6a[S12]	23.2	12.0 (296K)		
HOF 1a[S13]	42.18	30.19		
PB-1[S14]	38.28	≈20		
PB-2[S15]	74.25	<45		
CPOC-H_2[S16]	28.52	22.27		
CPOC-Co[S17]	22.41	18.37		
Fe-PB[S18]	29.79	20.43		
Ni-TCPP[S19]	11.51	8.13		
Ni-TCPP-TPyP[S20]	24.50	19.09		

Selectivity Prediction for Binary Mixture Adsorption: Ideal adsorbed solution theory (IAST)

The Ideal Adsorbed Solution Theory (IAST) was employed to predict the adsorption of binary mixtures based on the experimental pure-gas isotherms. To apply IAST, the single-component isotherms must first be fitted to an appropriate model. While there are no strict limitations on the choice of model for fitting the adsorption isotherm, it is crucial to ensure a precise fit over the pressure range being studied. Various isotherm models were evaluated for the quality of fit to the experimental isotherms of N_2 and CO_2 at 273 K and 298 K, with the dual-site Langmuir equation providing the best match to the experimental data.

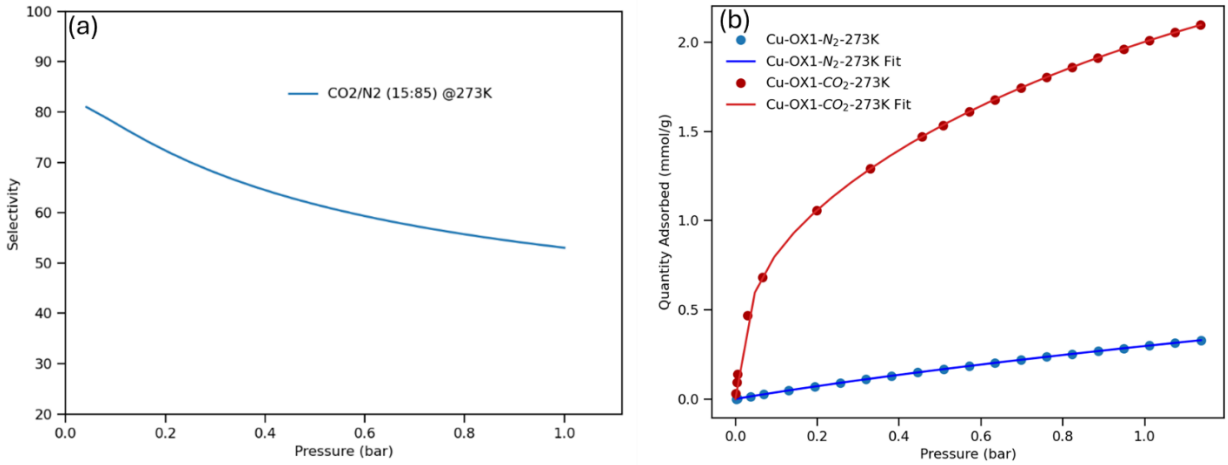

Figure S37 (a) IAST predicted selectivity for CO_2/N_2 in Cu-OX1 (**1**) at 273 K; (b) Gas adsorption isotherms and dual-site Langmuir fit curves for N_2 and CO_2 in Cu-OX1 (**1**) at 273 K.

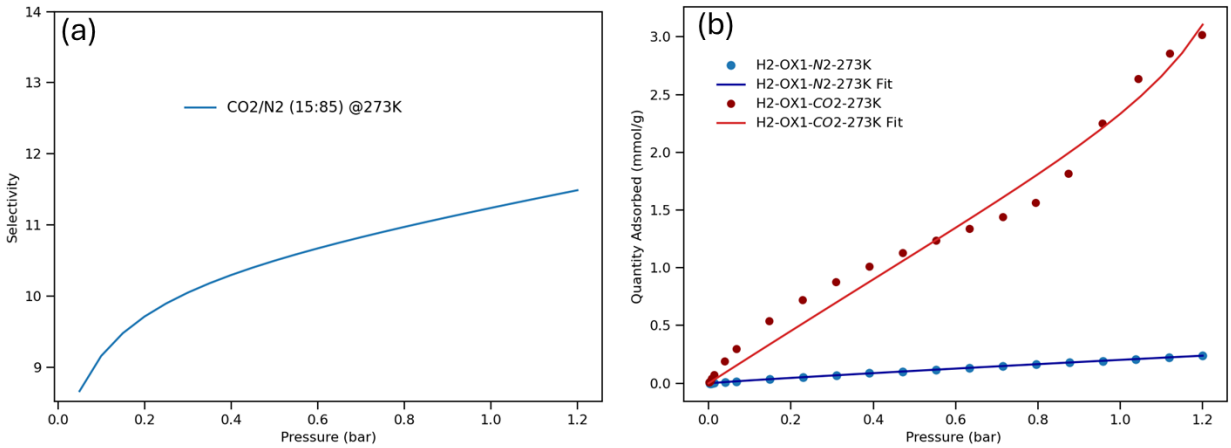

Figure S38 (a) IAST predicted selectivity for CO_2/N_2 in H2-OX1 (**2**) at 273 K; (b) Gas adsorption isotherms and dual-site Langmuir fit curves for N_2 and CO_2 in H2-OX1 (**2**) at 273 K.

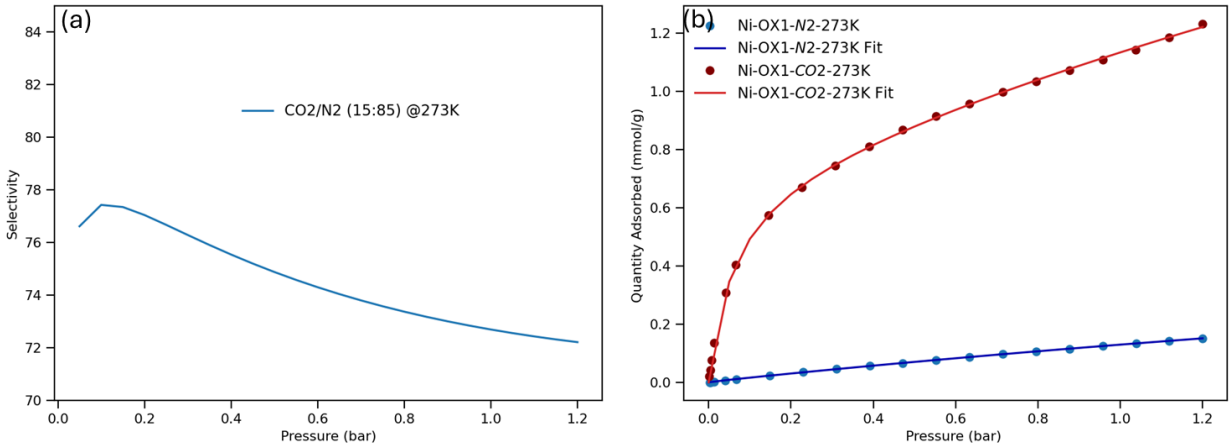

Figure S39 (a) IAST predicted selectivity for CO_2/N_2 in Ni-OX1 (**3**) at 273 K; (b) Gas adsorption isotherms and dual-site Langmuir fit curves for N_2 and CO_2 in Ni-OX1 (**3**) at 273 K.

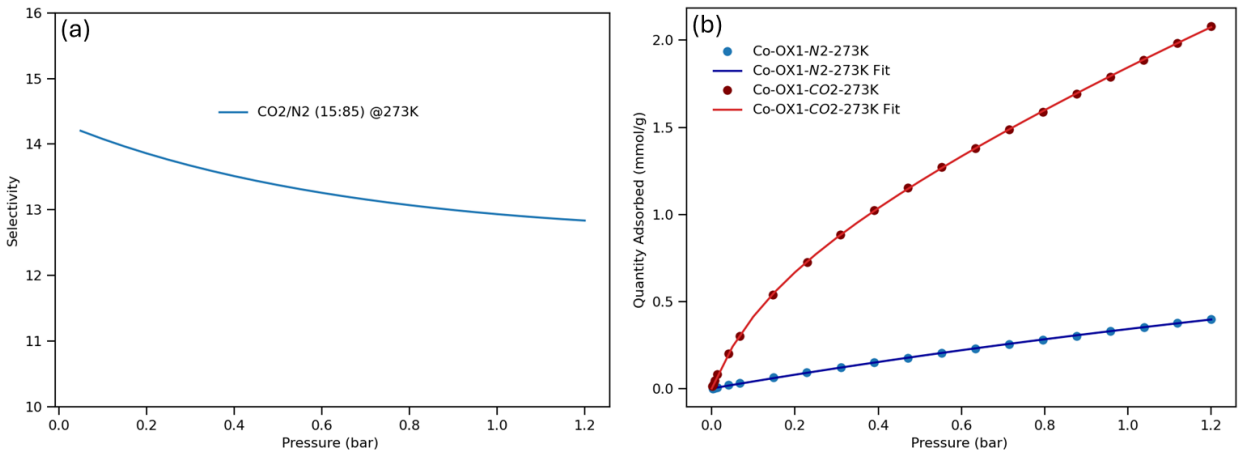

Figure S40 (a) IAST predicted selectivity for CO_2/N_2 in Co-OX1 (**4**) at 273 K; (b) Gas adsorption isotherms and dual-site Langmuir fit curves for N_2 and CO_2 in Co-OX1 (**4**) at 273 K.

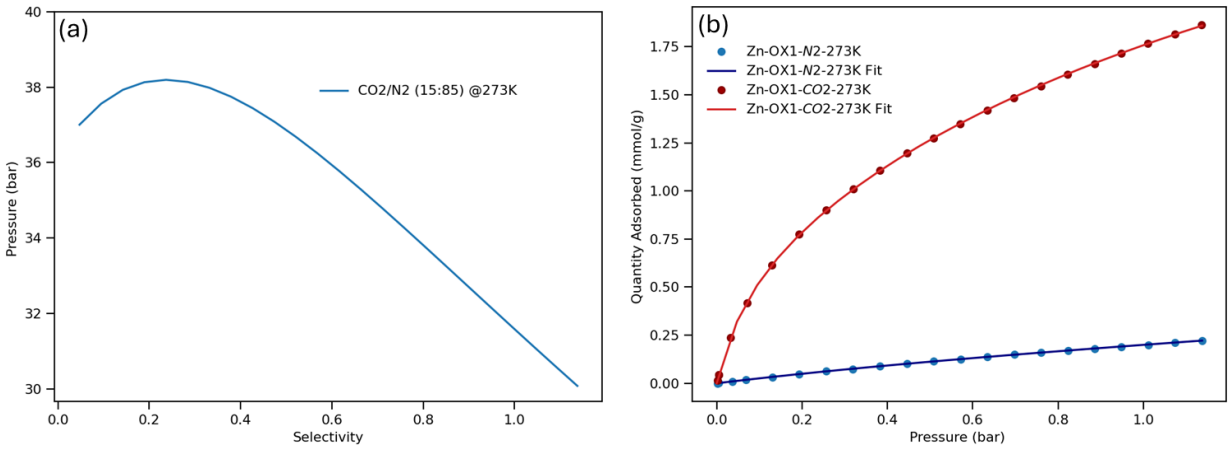

Figure S41 (a) IAST predicted selectivity for CO_2/N_2 in Zn-OX1 (**5**) at 273 K; (b) Gas adsorption isotherms and dual-site Langmuir fit curves for N_2 and CO_2 in Zn-OX1 (**5**) at 273 K.

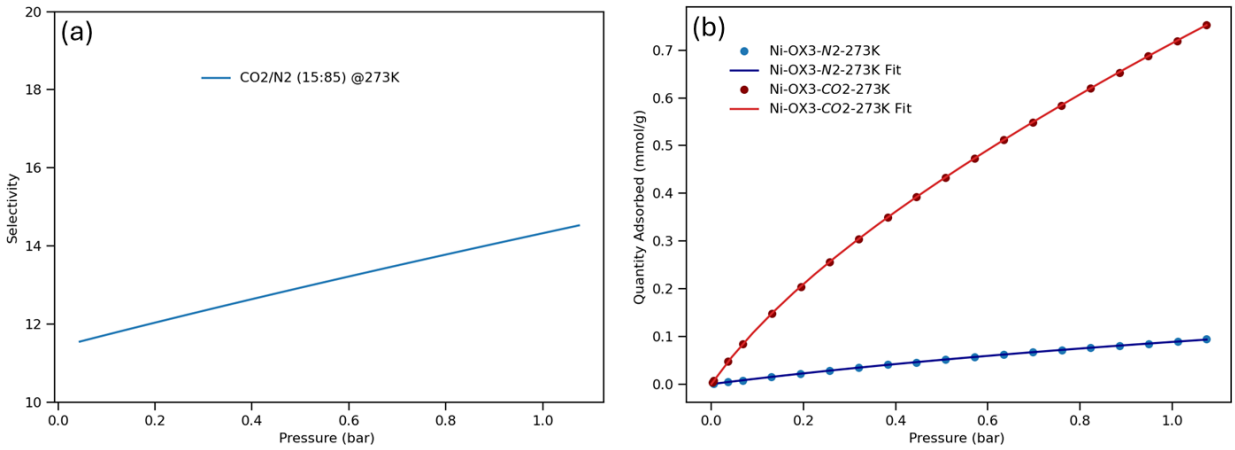

Figure S42 (a) IAST predicted selectivity for CO_2/N_2 in Ni-OX3 (**6**) at 273 K; (b) Gas adsorption isotherms and dual-site Langmuir fit curves for N_2 and CO_2 in Ni-OX3 (**6**) at 273 K.

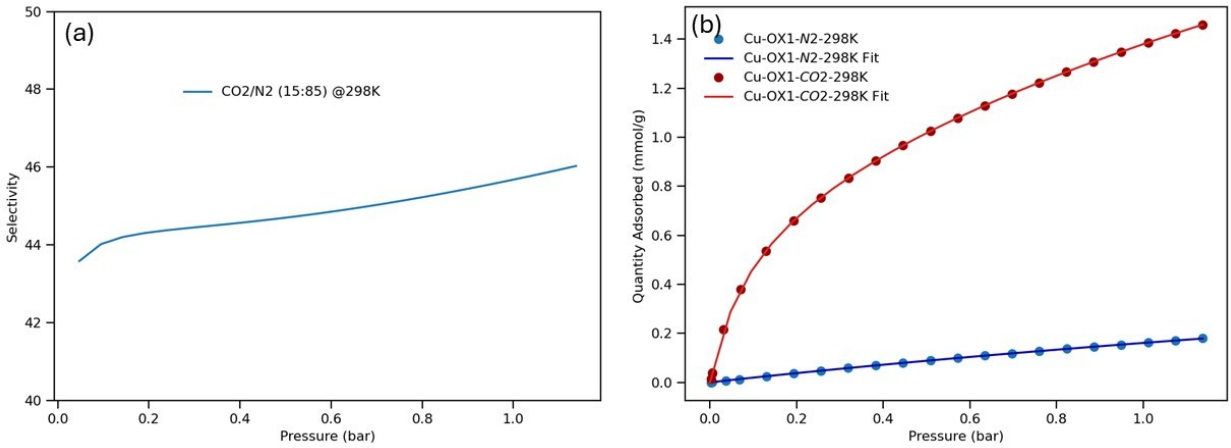

Figure S43 (a) IAST predicted selectivity for CO_2/N_2 in Cu-OX1 (**1**) at 298 K; (b) Gas adsorption isotherms and dual-site Langmuir fit curves for N_2 and CO_2 in Cu-OX1 (**1**) at 298 K.

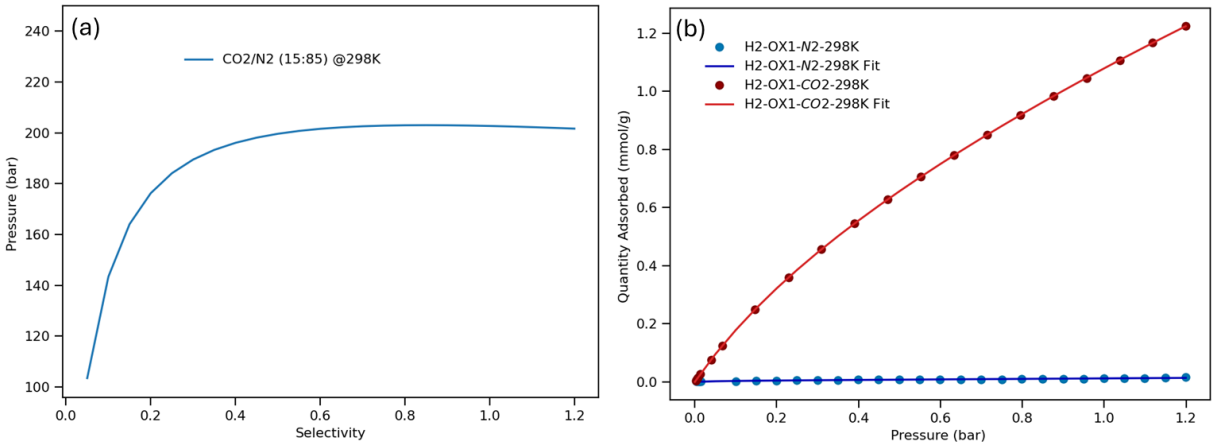

Figure S44 (a) IAST predicted selectivity for CO_2/N_2 in H2-OX1 (**2**) at 298 K; (b) Gas adsorption isotherms and dual-site Langmuir fit curves for N_2 and CO_2 in H2-OX1 (**2**) at 298 K.

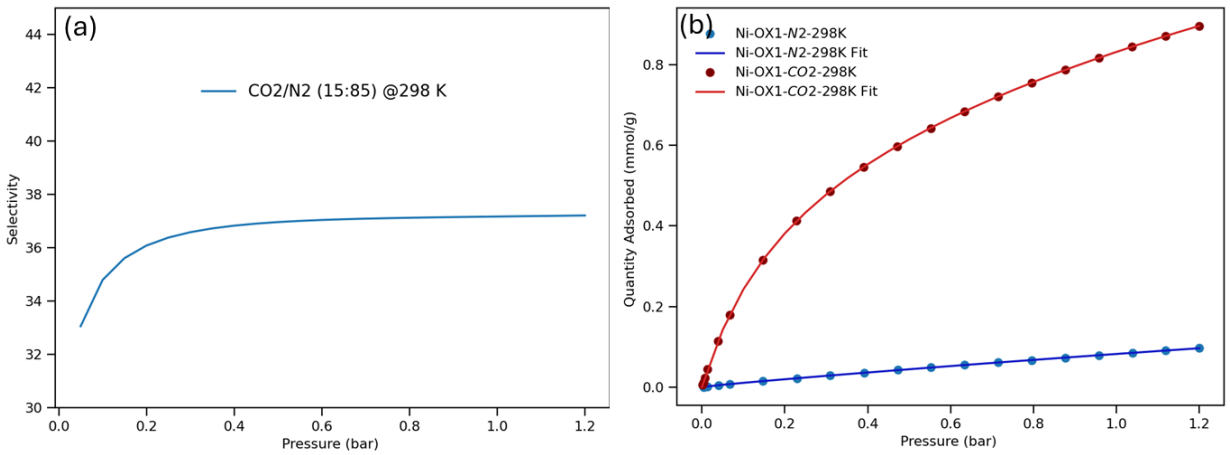

Figure S45 (a) IAST predicted selectivity for CO_2/N_2 in Ni-OX1 (**3**) at 298 K; (b) Gas adsorption isotherms and dual-site Langmuir fit curves for N_2 and CO_2 in Ni-OX1 (**3**) at 298 K.

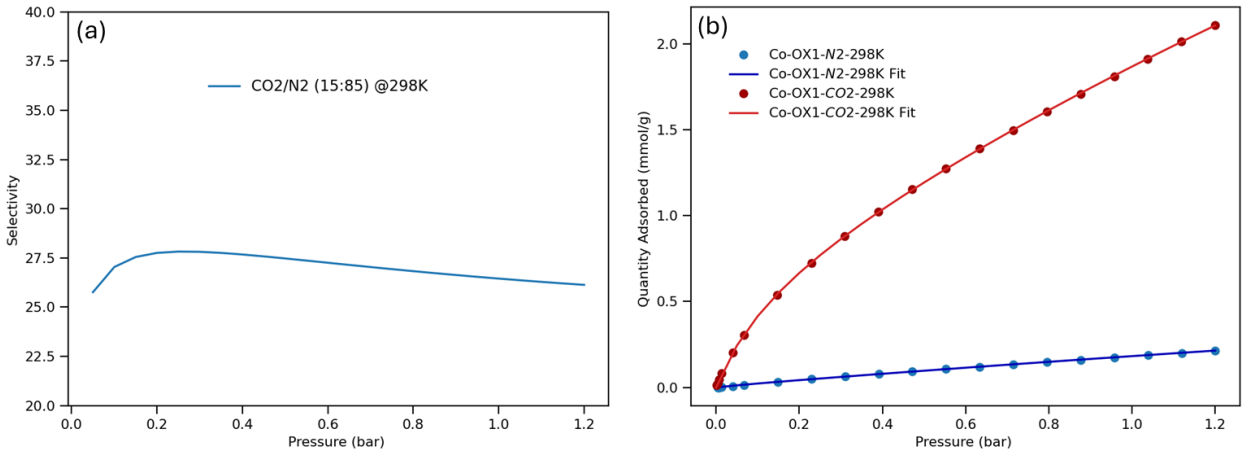

Figure S46 (a) IAST predicted selectivity for CO_2/N_2 in Co-OX1 (**4**) at 298 K; (b) Gas adsorption isotherms and dual-site Langmuir fit curves for N_2 and CO_2 in Co-OX1 (**4**) at 298 K.

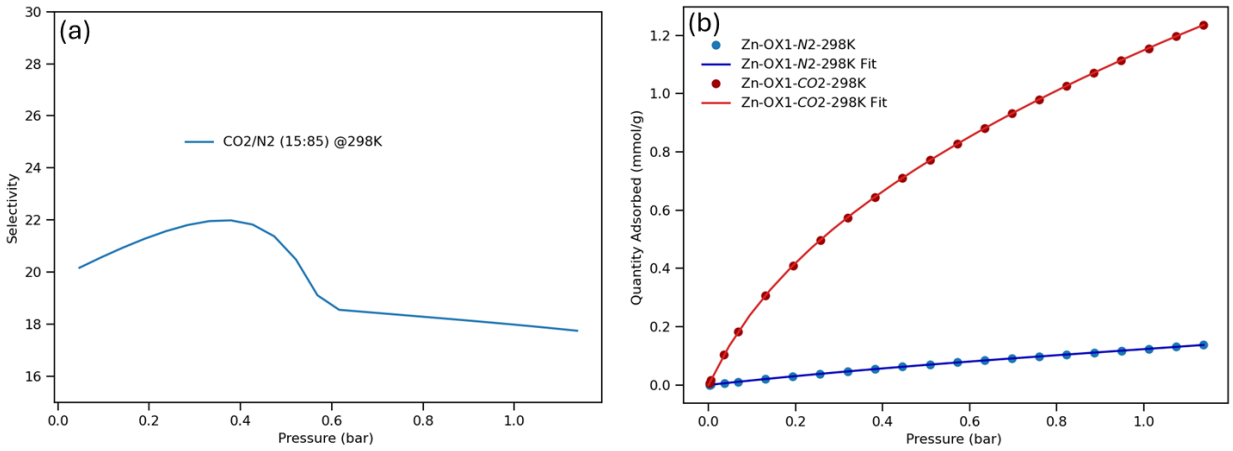

Figure S47 (a) IAST predicted selectivity for CO_2/N_2 in Zn-OX1 (**5**) at 298 K; (b) Gas adsorption isotherms and dual-site Langmuir fit curves for N_2 and CO_2 in Zn-OX1 (**5**) at 298 K.

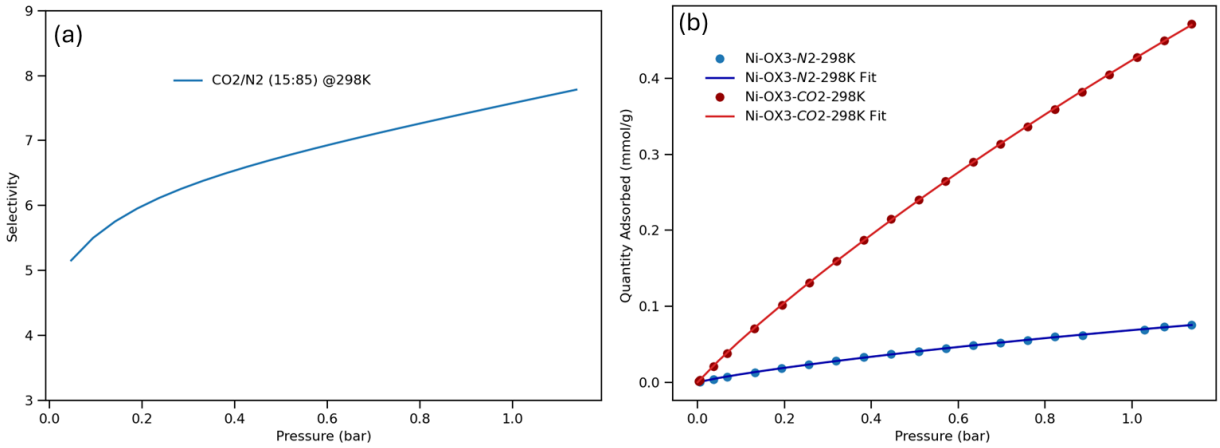

Figure S48 (a) IAST predicted selectivity for CO_2/N_2 in Ni-OX3 (**6**) at 298 K; (b) Gas adsorption isotherms and dual-site Langmuir fit curves for N_2 and CO_2 in Ni-OX3 (**6**) at 298 K.

References:

S1. M. K. Chahal and M. Sankar, *Dalton Trans.*, 2016, **45**, 16404–16412.

S2. M. K Chahal, S. Maji, A. Liyanage, Y. Matsushita, P. Tozman, D. T. Payne, W. Jevasuwan, N. Fukata, P. A. Karr, J. Labuta, L. K. Shrestha, S. Ishihara, K. Ariga, F. D'Souza, G. Yoshikawa, Y. Yamauchi and J. P Hill, *Mater. Chem. Front.*, 2023, **7**, 325–332.

S3. M. K Chahal, A. Liyanage, A. Z. Alsaleh, P. A. Karr, J. P. Hill and F. D'Souza, *Chem. Sci.*, 2021, **12**, 4925–4930.

S4. CrystalClear (Rigaku Corporation, Tokyo, 2005).

S5. Sheldrick, G. M. SHELXT – Integrated space-group and crystal-structure determination. Acta Cryst. A71, 3–8 (2015).

S6. Sheldrick, G. M. A short history of SHELX. Acta Cryst. A64, 112–122 (2008).

S7. Farrugia, L. J. WinGX suite for small-molecule single-crystal crystallography. J. Appl. Cryst. 32, 837–838 (1999).

S8. Y. Wang, D. Liu, J. Yin, Y. Shang, J. Du, Z. Kang, R. Wang, Y. Chen, D. Sun and J. Jiang, *Chem. Commun.*, 2020, **56**, 703–706.

S9. C. Wang, X. Song, Y. Wang, R. Xu, X. Gao, C. Shang, P. Lei, Q. Zeng, Y. Zhou, B. Chen and P. Li, *Angew. Chem. Int. Ed.*, 2023, 62, e202311482.

S10. Q.Yin, J. Lü, H.-F. Li, T.-F. Liu and R. Cao, *Cryst. Growth Des.*, 2019, **19**, 4157–4161.

S11. W. Yang, B. Li, H. Wang, O. Alduhaish, K. Alfooty, M. A. Zayed, P. Li, H. D. Arman and B. Chen, *Cryst. Growth Des.* 2015, **15**, 2000–2004.

S12. W. Yang, F. Yang, T.-L. Hu, S. C. King, H. Wang, H. Wu, W. Zhou, J.-R. Li, H. D. Arman and B. Chen, *Cryst. Growth Des.*, 2016, **16**, 5831–5835.

S13. Z. Zhang, J. Li, Y. Yao and S. Sun, C*ryst. Growth Des.*, 2015, **15**, 5028–5033.

S14. S. Hong, Md. R. Rohman, J. Jia, Y. Kim, D. Moon, Y. Kim, Y. H. Ko, E. Lee and K. Kim, *Angew. Chem. Int. Ed.*, 2015, **54**, 13241–13244.

S15. X. Liu, C. Liu, X. Song, X. Ding, H. Wang, B. Yu, H. Liu, B. Han, X. Li and J. Jiang, *Chem. Sci.*, 2023, **14**, 9086–9094.

S16. P. T. Smith, B. P. Benke, Z. Cao, Y. Kim, E. M. Nichols, K. Kim, and C. J. Chang, *Angew. Chem. Int. Ed.*, 2018, **57**, 9684 –9688.

S17. Y. Zhang, P. Li, P. Cui, X. Hu, C. Shu, R. Sun, M. Peng, B. Tan and X. Wang, *Angew. Chem. Int. Ed.*, 2024, **63**, e202413131.